Summer 8-16-2024

A Temperature Compensated Lateral Field Excited Lithium Tantalate Sensor Platform

Yuri Trusty
University of Maine, yuri.trusty@maine.edu

A TEMPERATURE COMPENSATED LATERAL FIELD EXCITED LITHIUM TANTALATE SENSOR PLATFORM

By

Yuri Trusty

B.S. University of Maine, 2022

A THESIS

Submitted in Partial Fulfillment of the

Requirements for the Degree of

Master of Science

(in Electrical Engineering)

The Graduate School

The University of Maine

August 2024

Advisory Committee:

John F. Vetelino, Professor of Electrical and Computer Engineering, Advisor

Nuri Emanetoglu, Associate Professor of Electrical and Computer Engineering

Mauricio Pereira da Cunha, Professor of Electrical and Computer Engineering

UNIVERSITY OF MAINE GRADUATE SCHOOL LAND ACKNOWLEDGMENT

The University of Maine recognizes that it is located on Marsh Island in the homeland of Penobscot people, where issues of water and territorial rights, and encroachment upon sacred sites, are ongoing. Penobscot homeland is connected to the other Wabanaki Tribal Nations—the Passamaquoddy, Maliseet, and Micmac—through kinship, alliances, and diplomacy. The University also recognizes that the Penobscot Nation and the other Wabanaki Tribal Nations are distinct, sovereign, legal and political entities with their own powers of self-governance and self-determination.

A TEMPERATURE COMPENSATED LATERAL FIELD EXCITED

LITHIUM TANTALATE SENSOR PLATFORM

By Yuri Nikolis Trusty

Thesis Advisor: Dr. John F. Vetelino

An Abstract of the Thesis Presented
In Partial Fulfillment of the Requirements for the
Degree of Master of Science
(in Electrical Engineering)
August 2024

The most common bulk acoustic wave (BAW) sensing platform is the AT-cut quartz crystal microbalance (QCM), which exhibits a pure transverse shear mode (TSM) that is temperature compensated near room temperature. Due to the inability of shear waves to propagate in liquids, a pure TSM is desirable for applications such as biosensing, where the target is typically detected from within a fluid. Resonant BAW modes that are thickness field excited (TFE) by electrodes on both major faces of the crystal substrate, prevent electrical property detection at the sensing surface. In contrast, lateral field excitation (LFE) only requires electrodes on a single face of the substrate, leaving the sensing surface bare. This difference results in sensitivity to changes in both mechanical and electrical properties.

Theory and preliminary experimentation have indicated that, via LFE, a temperature compensated pure TSM also exists near the Z-cut of lithium tantalate ($LiTaO_3$). With

electromechanical coupling several times greater than that of quartz, an LFE $LiTaO_3$ sensor may provide superior sensitivity for detecting minute variations in measurands, such as the biomarkers associated with certain cancers.

This work involves the theoretical and experimental search for a $LiTaO_3$ orientation which has an LFE pure TSM that is temperature compensated at room temperature. A set of orientations ranging from (YXwl) 0°/-85° to 0°/-90° was chosen for experimental verification and a method for temperature characterization of LFE $LiTaO_3$ BAW resonances was developed. The resonant frequency temperature response of each sample was shown to be parabolic, with a linear relationship between crystal orientation angle and temperature inflection point, i.e. turnaround temperature. Specifically, the (YXwl) 0°/-87° cut with a turnaround temperature at 26.4°C demonstrates that a pure TSM in $LiTaO_3$, that is temperature compensated near room temperature, can be excited via LFE. For this $LiTaO_3$ cut, the temperature coefficient of frequency (TCF), defined as the derivative of resonant frequency shift with respect to temperature, is a linear function of temperature that is zero-valued at 26.4°C. In contrast, the cubic resonant frequency temperature response of AT-cut quartz results in a parabolic TCF curve with an inflection point at room temperature and less resonant frequency shift per °C in the vicinity of room temperature. Although the parabolic temperature characteristic of $LiTaO_3$ does not grant the degree of temperature stability provided by the cubic temperature characteristic of AT-cut quartz, the LFE TSM in $LiTaO_3$ has a piezoelectric coupling that is nearly seven times higher than that of the room temperature compensated LFE mode in AT-cut quartz [1]. This higher coupling may contribute to a sensor with increased dynamic range and possibly increased sensitivity. Future work focusing on the development of an $LiTaO_3$ sensing platform

could profoundly impact sensor systems in agriculture, homeland security, global warming, and medical applications.

ACKNOWLEDGEMENTS

This research was supported by NSF grant 1851998 REU Site: Sensor Science and Engineering, the University of Maine's Frontier Institute for Research in Sensor Technologies (FIRST), as well as the Electrical and Computer Engineering Department. $LiTaO_3$ samples were supplied by Hangzhou Freqcontrol Electronic Technology LTD. and Yamaju Ceramics Co. I would like to thank Dr. John Vetelino for providing me with the opportunity to engage in this work and his guidance throughout the process. I would also like to extend my gratitude to Dr. Nuri Emanetoglu for his persistent encouragement and constant guidance, which cannot be overstated. Thank you to Dr. Mauricio Pereira da Cunha as well, for providing his expertise and invaluable technical feedback. Many thanks are also due to Jason McGann and Jequil Hartz, for sharing their knowledge and providing mentorship. I would be remiss if I didn't thank Dr. George Bernhardt, Michael Call, and Ekaterina Khmeleva for their abundant assistance in the lab. Lastly, I would like to thank my family, whose unrelenting patience, support, and inspiration made this possible.

TABLE OF CONTENTS

CHAPTER 1

INTRODUCTION

1.1 Background and Motivation

A sensor system consists of three primary components: sample preparation, the sensing element, and the read-out electronics. Figure 1-1 illustrates the components of a typical target-capture sensor system.

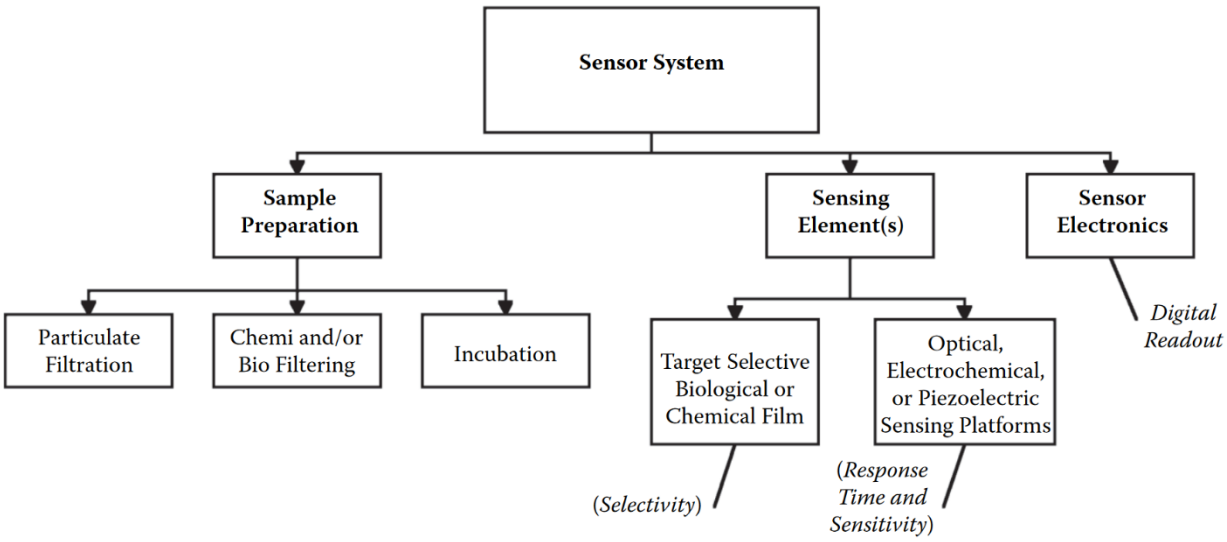

Figure 1-1. Functional block diagram of a typical target-capture sensor system [8].

Sample preparation provides the first level of selectivity to the sensor system. Sample preparation may involve chemical and/or biological filtering of potential interferents, as well as incubation of the target analyte to be presented to the next component, the sensing element. The sensing element typically consists of a measurand selective chemical or biological film deposited on a sensing platform. This selective film is designed such that sorption of the target measurand may alter its optical, electrical, and/or mechanical properties. The sensor platform is chosen to be sensitive to one or more of these film property changes. Finally, the read-out

electronics interface with the sensor element and are responsible for processing and conveying the sensor response to the observer. The focus of this thesis is on the sensor platform, a key component in the sensing element.

Most commercial sensing platforms and related techniques in use are capable of only detecting electrical or mechanical property changes using a target selective film. Surface plasmon resonance, for example, detects changes at the sensing surface by monitoring optical properties such as reflectance, transmission or absorption [19]. Electrochemical platforms usually consist of a metal oxide deposited on an insulator and can detect changes in conductivity [8]. A third type of platform, and the focus of this thesis, is the piezoelectric acoustic wave sensing platform. In this platform, an acoustic wave is excited in a piezoelectric crystal [8]. The frequency of this wave changes in response to electrical and/or mechanical property changes in the measurand selective film. In a surface acoustic wave (SAW) sensing platform excites SAWs that propagate along the surface of the crystal substrate, including the selective film, are excited. In a bulk acoustic wave (BAW) sensing platform, resonant acoustic waves that travel through the bulk of the piezoelectric substrate are excited, interacting with the sensing surface as the reflective boundary surface.

One of the most common BAW sensing platforms is the quartz crystal microbalance (QCM), which employs a transverse shear acoustic wave to probe the sensing surface. An important property of the transverse shear mode (TSM) is that the material's particle displacements are perpendicular to the direction of the wave propagation along the thickness of the piezoelectric crystal. This makes the BAW TSM particularly suited for liquid and gas-phase sensing applications, as shear waves do not effectively propagate through a liquid, thus reducing

acoustic energy losses at the sensing surface. Additionally, the crystallographic orientation of AT-cut quartz used in the QCM exhibits significant temperature stability of the BAW frequency in the vicinity of room temperature. This is known as room temperature compensation [8].

The BAW mode is typically excited within the QCM via thickness field excitation (TFE), with electrodes placed on the top and bottom of the crystal substrate [7]. However, this results in a fundamental limitation of the TFE QCM, in that the electrode on the sensing surface prevents detection of electrical property changes in the sensing film. Thus, the classic QCM is only capable of detecting changes in mechanical properties, such as mass or viscoelasticity. AT-cut quartz also has a relatively low piezoelectric coupling coefficient compared with other piezoelectric materials such as lithium niobate or lithium tantalate. This results in a sensing system with limited sensitivity to changes in electrical properties and possibly a reduced dynamic range relative to noise levels.

In contrast to the TFE configuration, lateral field excitation (LFE) employs electrodes only on the backside of the sensing platform, leaving the sensing surface bare. Work on LFE has shown that it is possible to excite a BAW TSM while still allowing for detection of changes in both mechanical and electrical properties, such as conductivity or permittivity, in the measurand selective film [2-3, 11, 20-25]. The ability to detect both types of changes could result in higher sensitivity.

1.2 Thesis Objectives and Organization

The limited piezoelectric coupling of AT-cut quartz and the insensitivity of the TFE configuration to electrical signals have motivated the search for piezoelectric materials with

higher piezoelectric coupling than quartz and that can support a temperature compensated bulk TSM using the LFE configuration. Previous work using a theoretical search has identified lithium tantalate ($LiTaO_3$) as one such candidate material. The objective of this thesis is to identify a specific crystallographic orientation of $LiTaO_3$ (LT) that supports a room temperature compensated lateral field excited transverse shear mode, which can then be incorporated into a sensor system and can act as an alternative to the quartz in the QCM. The present work involved theoretical calculations to predict a temperature compensated cut, based on previously published work [22] as well as experimental demonstration of the cut. The first set of experiments compared the stability of the LFE BAW responses in white (untreated) LT with black (treated to reduce pyroelectricity) LT. Next, LT crystals from several vendors in China and Japan were compared to ensure they were of similar quality. Finally, a methodical search was conducted to identify the precise cut of LT for a room temperature compensated LFE BAW. The discrepancy between the theoretical model and the experimental results, which is discussed in Chapter 4, is hypothesized to be a result of the fact that the material constants used the theoretical calculations were determined using crystals grown in the 1970s, whereas the experimental work in this thesis was done on LT samples grown in 2020.

In Chapter 2 of this thesis, theoretical background will be provided for piezoelectric materials, bulk acoustic waves, thickness and lateral field excitation, and temperature compensation. The calculation of bulk acoustic wave properties of piezoelectric crystals will be based on the quasi-static approximation. In Chapter 3, the theoretical model for LFE developed using MATLAB will be presented and results of simulations used to identify the desired crystallographic orientations of LT will be discussed. In Chapter 4, experimental work with

several cuts of LT will be described and the results will be discussed. Finally, this thesis will be concluded in Chapter 5 with a summary of results and discussion of future work.

CHAPTER 2

THEORETICAL BACKGROUND

2.1 Piezoelectric Materials

Piezoelectricity is the property of certain materials whereby an applied mechanical stress induces an electric field within the material. Similarly, an electric field applied to the same material generates a mechanical strain within it [8]. These phenomena are known as the direct piezoelectric effect and the converse piezoelectric effect, respectively. Piezoelectricity occurs in twenty of the thirty-two crystal classes whose unit cells are hemimorphic, possessing no center of symmetry [6]. It is this asymmetric distribution of electric charge within piezoelectric materials' crystal structure which permits an electric potential to develop in response to mechanical force and a mechanical strain to develop in response to an electric force field. This ability to convert mechanical energy to electrical energy and vice versa has resulted in piezoelectric materials finding applications in many fields. In the medical field, for example, ultrasound transducers are typically formed from piezoelectric ceramics such as lead zirconium titanate (PZT) [26]. As another example, quartz, the most common piezoelectric crystal, has been used in wrist watches, computer clocks, crystal radios, radio frequency (RF) signal processing, sensors such as the QCM, and many other applications [7].

2.2 Bulk Acoustic Wave Devices for Analyte Detection

Piezoelectric crystal plate resonators form the basis of bulk acoustic wave (BAW) sensing platforms [8]. Operating on the principle of the converse piezoelectric effect, electrodes placed on the crystal plate supply an alternating electric field, which excites resonant BAW modes within the bulk of the crystal [8]. The presence of a target analyte at the crystal plate's sensing

surface results in a target-capture event between the target and the measurand selective film, which in turn can result in mechanical or electrical perturbations at the sensing surface. These perturbations at the sensing surface induce shifts in the crystal's resonant frequency. By monitoring these frequency shifts, concentrations of the target analyte may be detected and measured.

2.2.1 Bulk Acoustic Wave Thickness Modes

The BAW modes excited in the piezoelectric crystal plate have mechanical displacements whose properties depend on the wave propagation direction within the crystal. Propagation can occur along any direction and can be expressed in an orthogonal coordinate system. Piezoelectric crystal plates implemented in BAW devices are chosen such that the BAW modes' directions of propagation are aligned with the plate's thickness dimension, which is significantly smaller than its lateral dimensions. There are three of these thickness modes with BAW propagation direction parallel to crystal plate thickness, and they are labeled according to the particle motion with respect to wave propagation direction. The longitudinal, or quasi-longitudinal, mode possesses the highest acoustic phase velocity and produces mechanical displacement that is parallel, or predominantly parallel, to its wave propagation direction. The other two thickness modes are both shear, or quasi-shear, modes which both produce mechanical displacement that is perpendicular, or predominantly perpendicular, to wave propagation direction. These two shear modes are typically designated as slow and fast, depending on their acoustic phase velocities relative to one another. Figure 2-1 illustrates the three thickness BAW modes in an example of an AT-cut quartz plate which was cut from a larger crystal with a corresponding unprimed orthogonal crystallographic coordinate system.

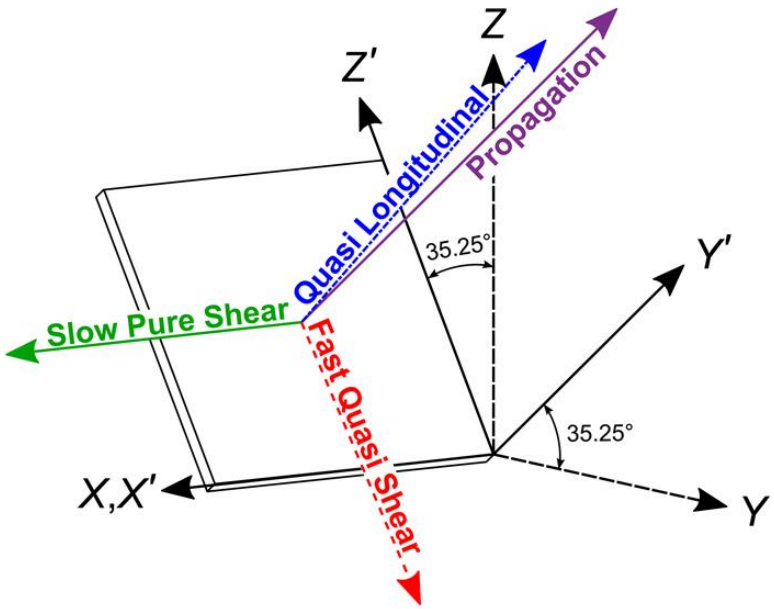

Figure 2-1. AT-cut quartz crystal plate with thickness mode displacement polarizations [7].

The AT-cut plate in Figure 2-1 relates to the primed orthogonal coordinate system which is defined by a 35.25° rotation about the X-axis of the original unprimed coordinate system. It can also be seen in Figure 2-1 that the wave propagation of the three thickness modes is collinear with the crystal plate's thickness, in the Y' direction. Moreover, the longitudinal mode is quasi because its displacement polarization (blue) is not purely parallel to its propagation direction, but at some intermediate polarization between parallel and perpendicular to wave propagation direction. Similarly, the fast shear mode (red) is also quasi as its displacement is not purely polarized perpendicularly to wave propagation direction. The slow shear (green), however, is a pure shear mode because it produces displacement in the crystal with is purely perpendicular to its propagation direction.

2.2.2 Transverse Shear Mode

Shear modes are particularly suited for liquid and gas-phase sensing as they do not radiate effectively into these media. Therefore, the acoustic energy will not be significantly transmitted into the liquid or gas phase sensing medium, minimizing compromise of the resonator quality factor. The optimal performance of a BAW sensor for liquid media is thus dependent on the excitation of a pure transverse shear mode (TSM), whose propagation direction is through the thickness of the crystal plate, perpendicular to the sensing surface. Figure 2-2 illustrates the classic configuration of a BAW sensor device utilizing pure TSM.

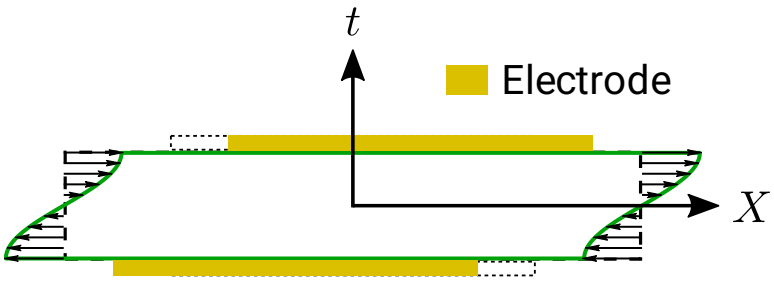

Figure 2-2. Pure TSM in a TFE BAW sensor.

As shown in Figure 2-2, the classic configuration of BAW sensor devices, like the QCM for example, places electrodes on both faces of the crystal plate. An alternating electric field is then conveyed through the crystal plate's thickness to excite the resonant pure TSM. Mechanical displacement is collinear with the X-axis in Figure 2-2, as shown by the deformation of the crystal plate (green), and BAW propagation direction is collinear with the t-axis (crystal plate thickness). This electrode configuration is known as thickness field excitation (TFE).

2.2.3 Thickness Field Excitation and Lateral Field Excitation

The method by which resonant pure TSMs are excited is central to the classification of BAW sensing platforms. TFE, shown in Figure 2-2 and Figure 2-3, employs electrodes on both major faces of the crystal plate, and the exciting electric field is conveyed through the thickness of the plate. Figure 2-3 also illustrates lateral field excitation (LFE), where both electrodes occupy a single face of the crystal plate, and the exciting electric field is applied mostly across the gap between the electrodes.

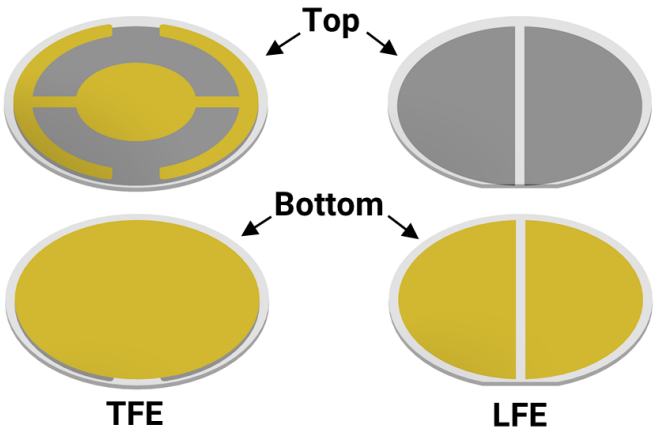

Figure 2-3. TFE (left) and LFE (right) BAW sensor configurations.

The electric field produced via TFE cannot significantly interact with the sensing environment due to the conducting electrode shielding the sensing surface. As a result, the measurement of electrical property changes such as relative permittivity and conductivity is not possible [9-10]. In contrast, an LFE device possesses a bare sensing surface, thus, as can be seen in Figure 2-4, the electric field associated with the BAW mode can penetrate and interact with the sensing environment.

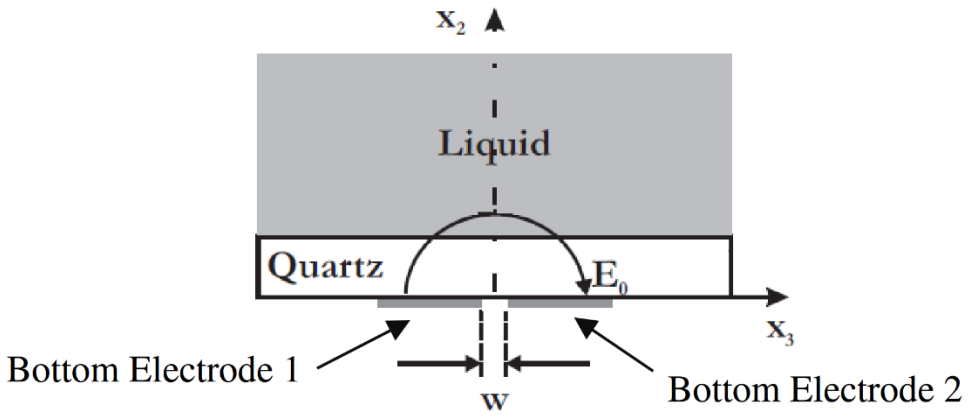

Figure 2-4. Electric field penetrating liquid medium at the surface of an LFE BAW sensor [1].

Because there is no shielding electrode at the LFE sensing surface, the electric field associated with the excited resonant BAW mode is sensitive to changes to electrical properties within the sensing environment. This allows sensing of not only mechanical property changes such as mass and viscoelasticity, but also electrical property changes such as relative permittivity and conductivity. An overall result of the LFE configuration has been shown to be an increase in sensitivity to both mechanical and electrical property changes [11].

2.2.4 Temperature Compensation

Excitation of a pure TSM within a piezoelectric BAW sensing platform is highly desirable for liquid and gas-phase sensing applications. Equally critical is the resonant frequency stability of the pure TSM with respect to temperature. Perhaps the most alluring characteristic of AT-cut quartz, and why it is used in the QCM as well as many other applications beyond sensing, is the fact that it is temperature compensated near 25° C, or room temperature. The resonant frequency of the pure TSM in AT-cut quartz has a cubic temperature characteristic and remains stable across a wide range of temperature variations centered around room temperature [12]. This is illustrated in Figure 2-5 below.

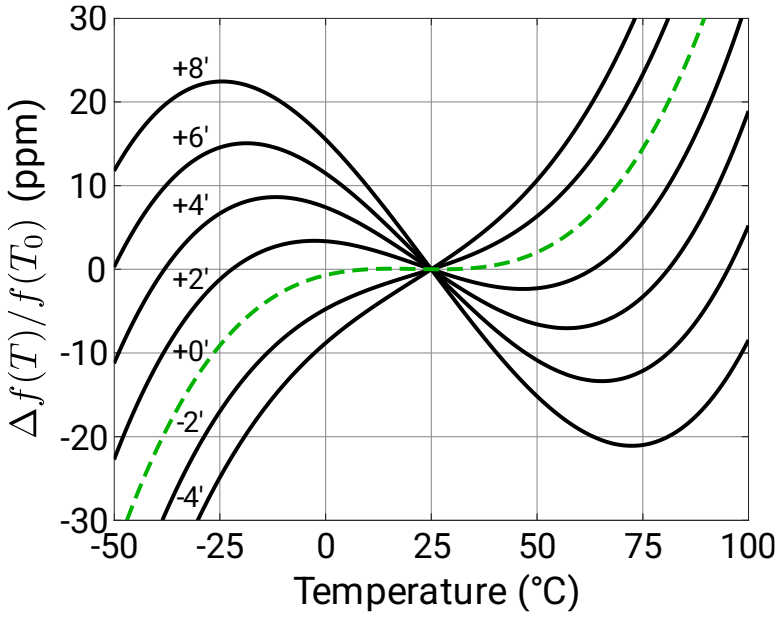

Figure 2-5. Temperature compensated shear mode behavior of (YXwl) 0°/-35° AT-cut quartz [7].

Frequency stability with respect to temperature means temperature variations negligibly impact a sensor's response. It allows a sensing system to be insensitive to ambient temperature fluctuations, thus crediting any response to changes of the target measurand.

2.3 Quasi-Static Approximation for Bulk Acoustic Wave Propagation

The propagation of acoustic waves in a piezoelectric crystal can be described by a combination of the Christoffel equation and Maxwell's equations. The Christoffel equation describes the dispersion of acoustic waves in a crystalline medium, relating the phase velocity of the acoustic waves to their propagation directions and the elastic and piezoelectric properties of the material. For piezoelectric materials, the Christoffel equation is modified to account for the additional coupling between mechanical strain and electric field. Solving the Christoffel equation determines the allowed modes of acoustic propagations in the crystal and calculates their phase velocities and polarization states.

Maxwell's equations describe the behavior of the electromagnetic fields in a given medium and their interaction with electric charges and currents. For piezoelectric crystals Maxwell's equations model the generation and propagation of electric fields resulting from mechanical strain-induced charge separations and the generation of mechanical strain due to applied electric fields. These equations, along with the appropriate boundary conditions, allow for the calculation of the electric fields induced by acoustic waves and the mechanical strain resulting from applied electric fields.

The complete analysis of acoustic wave propagation through a piezoelectric crystal using the Christoffel equation and Maxwell's equations is computationally cumbersome. However, the computation can be greatly simplified by adopting the quasi-static approximation. The quasi-static approximation assumes that the variation of the electric field within the crystal occurs slowly compared to the acoustic wavelength, which is valid as there are orders of magnitude of difference between the electromagnetic and acoustic wavelengths. A 6 MHz QCM, for example, operates with acoustic wavelengths on the order of millimeters and electromagnetic wavelengths on the order of tens of meters. Thus, it is valid to assume the variation of the electric field within the piezoelectric crystal is negligible compared with the acoustic field. As a result of this valid assumption, the electric field can be approximated to be constant over the spatial dimensions considered. Furthermore, since the electric field is assumed to be constant, the displacement currents are also assumed to be negligible, allowing the expression of Maxwell's equations in terms of only conduction currents.

Using the quasi-static approximation, the coupled acoustic and electromagnetic wave equations can be expressed as follows [14],

$$\frac{\delta T_{ij}}{\delta x_i} = \rho \frac{\delta^2 u_j}{\delta t^2} \tag{2.1}$$

and

$$\frac{\delta D_i}{\delta x_i} = 0 \quad . \tag{2.2}$$

Here, T_{ij} is the rank two stress tensor, ρ is the material density, u_j are the mechanical displacements, and D_i are the electric displacements. The i and j subscripts may be 1, 2, or 3 and represent the x, y, and z spatial components respectively.

The relationship of stress T_{ij} and electric displacement D_i to strain, S_{ij} and the electric field E_k is defined by the following constitutive equations [14],

$$T_{ij} = c_{ijkl}^{E} S_{kl} - e_{kij} E_k \tag{2.3}$$

and

$$D_i = e_{ikl} S_{kl} + \epsilon_{ik}^{S} E_k \tag{2.4}$$

where c_{ijkl}^{E}, e_{ikl}, and ϵ_{ik}^{S} are the tensors for the elastic, piezoelectric, and dielectric permittivity constants. The superscripts E and S in the elastic and dielectric constants indicate they are under a constant electric field and a constant strain respectively.

Although c_{ijkl}^{E} is a rank four tensor, the number of tensor elements can be reduced significantly as a result of symmetry. Because $T_{ij} = T_{ji}$ and $c_{ijkl}^{E} = c_{jikl}^{E}$, the number of elements is reduced from eighty-one to fifty-four. Similarly, because $S_{kl} = S_{lk}$ and $c_{ijkl}^{E} = c_{ijlk}^{E}$, the number of independent elements is further reduced to thirty-six. Furthermore, the abbreviated subscripts known as Voight indices can be used. They are summarized in Table 2-1 below.

Table 2-1. Subscript abbreviation with Voight indices.

I, J, K, L	*i, j, k, l*
1	*xx (11)*
2	*yy (22)*
3	*zz (33)*
4	*yz (23), zy (32)*
5	*zx (31), xz (13)*
6	*xy (12), yx (21)*

Thus, for example, Equation 2.3 can be written in tensor form as follows,

$$\begin{bmatrix} T_1 \\ T_2 \\ T_3 \\ T_4 \\ T_5 \\ T_6 \end{bmatrix} = \begin{bmatrix} c_{11}^E & c_{12}^E & c_{13}^E & c_{14}^E & c_{15}^E & c_{16}^E \\ c_{21}^E & c_{22}^E & c_{23}^E & c_{24}^E & c_{25}^E & c_{26}^E \\ c_{31}^E & c_{32}^E & c_{33}^E & c_{34}^E & c_{35}^E & c_{36}^E \\ c_{41}^E & c_{42}^E & c_{43}^E & c_{44}^E & c_{45}^E & c_{46}^E \\ c_{51}^E & c_{52}^E & c_{53}^E & c_{54}^E & c_{55}^E & c_{56}^E \\ c_{61}^E & c_{62}^E & c_{63}^E & c_{64}^E & c_{65}^E & c_{66}^E \end{bmatrix} \begin{bmatrix} S_1 \\ S_2 \\ S_3 \\ S_4 \\ S_5 \\ S_6 \end{bmatrix} - \begin{bmatrix} e_{11} & e_{21} & e_{31} \\ e_{12} & e_{22} & e_{32} \\ e_{13} & e_{23} & e_{33} \\ e_{14} & e_{24} & e_{34} \\ e_{15} & e_{25} & e_{35} \\ e_{16} & e_{26} & e_{36} \end{bmatrix} \begin{bmatrix} E_1 \\ E_2 \\ E_3 \end{bmatrix} \tag{2.5}$$

Finally, because of the symmetry of the elastic constant, i.e. $c_{IJ}^{E} = c_{JI}^{E}$, the number of independent terms in the tensor is further reduced from thirty-six to twenty-one.

The remaining acoustic and electromagnetic equations relating the strain to the displacement and the electric field to the electric potential, are as shown below [14].

$$S_{kl} = \frac{1}{2}\left(\frac{\delta u_k}{\delta x_l} + \frac{\delta u_l}{\delta x_k}\right) \tag{2.6}$$

and

$$E_k = -\frac{\delta \phi}{\delta x_k} \quad . \tag{2.7}$$

Substituting Equation 2.6 and Equation 2.7 into Equation 2.3 and then substituting that result into Equation 2.1 yields

$$\rho \frac{\delta^2 u_j}{\delta t^2} = c_{ijkl}^{E} \frac{\delta^2 u_k}{\delta x_i x_l} + e_{kij} \frac{\delta^2 \phi}{\delta x_i \delta x_k} \quad . \tag{2.8}$$

Similarly, we can substitute Equation 2.6 and Equation 2.7 into Equation 2.4, then substitute that result into Equation 2.2, and recognizing that $\frac{\delta^2 u_k}{\delta x_i \delta x_l} = \frac{\delta^2 u_l}{\delta x_i \delta x_k}$, the following equation results,

$$0 = e_{ikl} \frac{\delta^2 u_k}{\delta x_i \delta x_l} - \epsilon_{ik} \frac{\delta^2 \phi}{\delta x_i \delta x_k} \quad . \tag{2.9}$$

To solve Equation 2.8 and Equation 2.9, a plane wave is assumed to be propagating in the x_2 direction, along the thickness dimension of a crystal plate, in an orthogonal coordinate system as is illustrated in Figure 2-6 below.

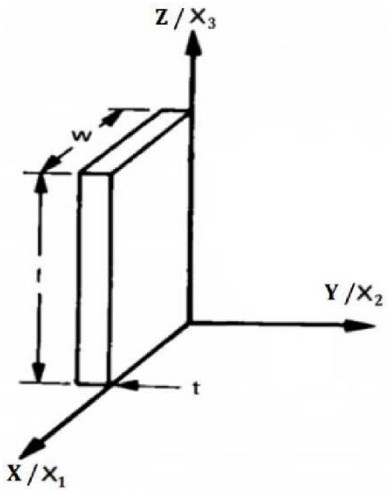

Figure 2-6. Unrotated piezoelectric crystal plate in an orthogonal coordinate system [1].

The solution for the plane wave propagating in x_2 direction is in the form,

$$u_j = \alpha_j e^{j(\kappa x_2 - \kappa v t)} \quad , \tag{2.10}$$

where κ is the wave vector and v the phase velocity. Because the wave is propagating in the x_2 direction,

$$\frac{\delta \phi}{\delta x_1} = \frac{\delta \phi}{\delta x_3} = 0 \tag{2.11}$$

and

$$\frac{\delta u_k}{\delta x_1} = \frac{\delta u_k}{\delta x_3} = 0 \quad . \tag{2.12}$$

Solving Equation 2.9 for $\frac{\delta^2 \phi}{\delta x_i \delta x_k}$ and substituting it into Equation 2.8 while also using Equation 2.11 and Equation 2.12 yields,

$$\rho \frac{\delta^2 u_j}{\delta t^2} = c'_{2jk2} \frac{\delta^2 u_k}{\delta x_2^2} \tag{2.13}$$

where c'_{2jk2} is the piezoelectrically stiffened elastic constant, defined as

$$c'_{2jk2} = c^E_{2jk2} + \frac{e_{22j} e_{2k2}}{\epsilon^S_{22}} \quad . \tag{2.14}$$

Finally, substituting Equation 2.10 into Equation 2.13 and expanding on subscripts k and j yields the set of three equations,

$$\begin{bmatrix} c'_{2112} & c'_{2122} & c'_{2132} \\ c'_{2212} & c'_{2222} & c'_{2232} \\ c'_{2312} & c'_{2322} & c'_{2332} \end{bmatrix} \begin{bmatrix} \alpha_1 \\ \alpha_2 \\ \alpha_3 \end{bmatrix} = \begin{bmatrix} \rho v^2 \alpha_1 \\ \rho v^2 \alpha_2 \\ \rho v^2 \alpha_3 \end{bmatrix} \quad , \tag{2.15}$$

where there are eigenvalues, c^m from the above stiffened elastic constant matrix that are associated with each of the three acoustic modes, with the superscript m indicating the mode. Each mode has displacement components α_1^m, α_2^m, and α_3^m and their associated phase velocities, v^m, are as follows,

$$v^m = \sqrt{\frac{c^m}{\rho}} \quad . \tag{2.16}$$

2.4 Thickness Field and Lateral Field Coupling Coefficients

For each acoustic mode there is a corresponding electromechanical coupling coefficient, K^2 [13]. The electromechanical coupling coefficient is an assessment of how well a piezoelectric material converts the supplied electrical energy to mechanical energy for a given acoustic mode. For TFE BAW configurations, the electromechanical coupling coefficient for a given acoustic mode is given by [14],

$$K_{TFE}^{(m)^2} = \frac{\left(\sum_{j=1}^{3} e_{22j}\beta_j^m\right)^2}{\epsilon_{22}^S c^m} \quad . \tag{2.17}$$

For given acoustic mode excited with the LFE BAW configuration, the electromechanical coupling coefficient is given by [15-16],

$$K_{LFE}^{(m)^2} = \frac{\left(\sum_{j=1}^{3}\left(e_{12j} - e_{22j}\frac{\epsilon_{12}^S}{\epsilon_{22}^S}\right)\beta_j^m\right)^2}{\left(\epsilon_{11}^S - \frac{\left(\epsilon_{12}^S\right)^2}{\epsilon_{22}^S}\right)c^m} \quad . \tag{2.18}$$

In Equation 2.17 and Equation 2.18 c^m and β_j^m are the eigenvalues and eigenvectors respectively from the stiffened elastic constant matrix in Equation 2.15.

2.5 Frequency Response Immittance Equations

The frequency response of idealized BAW resonators can be described by a set of immittance equations. Idealized BAW resonators are resonators for which the exciting electric fields are perfectly oriented in only the desired direction, the exciting electrodes possess zero mass, and there are no spurious acoustic modes present [1]. For a TFE BAW resonator, Equation

2.19 for electrical impedance below is theoretically suitable to describe its frequency response [15-16].

$$Z_{TFE}(\omega) = \frac{1}{j\omega C_0^{TFE}}\left(1 - \sum_{m=1}^{3} {K_{TFE}^{(m)}}^2 \frac{tan\left(\frac{\omega}{v_p^{(m)}}h\right)}{\frac{\omega}{v_p^{(m)}}h}\right) \quad (2.19)$$

The TFE series and parallel resonance frequencies, also known as the resonance and anti-resonance frequencies respectively, are described by the solutions to the following,

$$f_{TFE}^{s} \rightarrow \sum_{m=1}^{3} {K_{TFE}^{(m)}}^2 \frac{tan\left(\frac{\omega}{v_p^{(m)}}h\right)}{\frac{\omega}{v_p^{(m)}}h} = 1 \quad (2.20)$$

and

$$f_{TFE}^{p} \rightarrow \frac{\omega}{v_p^{(m)}}h = \frac{n\pi}{2}\ for\ n\ =\ 1, 3, 5, \ldots \quad (2.21)$$

For an LFE BAW resonator, it is theoretically suitable to describe its frequency response in terms of admittance [14, 16] as follows,

$$Y_{LFE}(\omega) = j\omega C_0^{LFE}\left(1 + \sum_{m=1}^{3} {K_{LFE}^{(m)}}^2 \frac{tan\left(\frac{\omega}{v_p^{(m)}}h\right)}{\frac{\omega}{v_p^{(m)}}h}\right) \quad (2.22)$$

The resonance and anti-resonance frequencies for the LFE BAW resonator are described by the solutions to Equation 2.23 and Equation 2.24 below, respectively.

$$f_{LFE}^{s} \rightarrow \frac{\omega}{v_p^{(m)}} h = \frac{n\pi}{2} \; for \; n \; = \; 1, 3, 5, \ldots \tag{2.23}$$

and

$$f_{LFE}^{p} \rightarrow \sum_{m=1}^{3} {K_{LFE}^{(m)}}^2 \frac{tan\left(\frac{\omega}{v_p^{(m)}} h\right)}{\frac{\omega}{v_p^{(m)}} h} = -1 \tag{2.24}$$

The idealized resonator frequency response in terms of impedance as described in Equation 2.19 is illustrated in Figure 2-7 below.

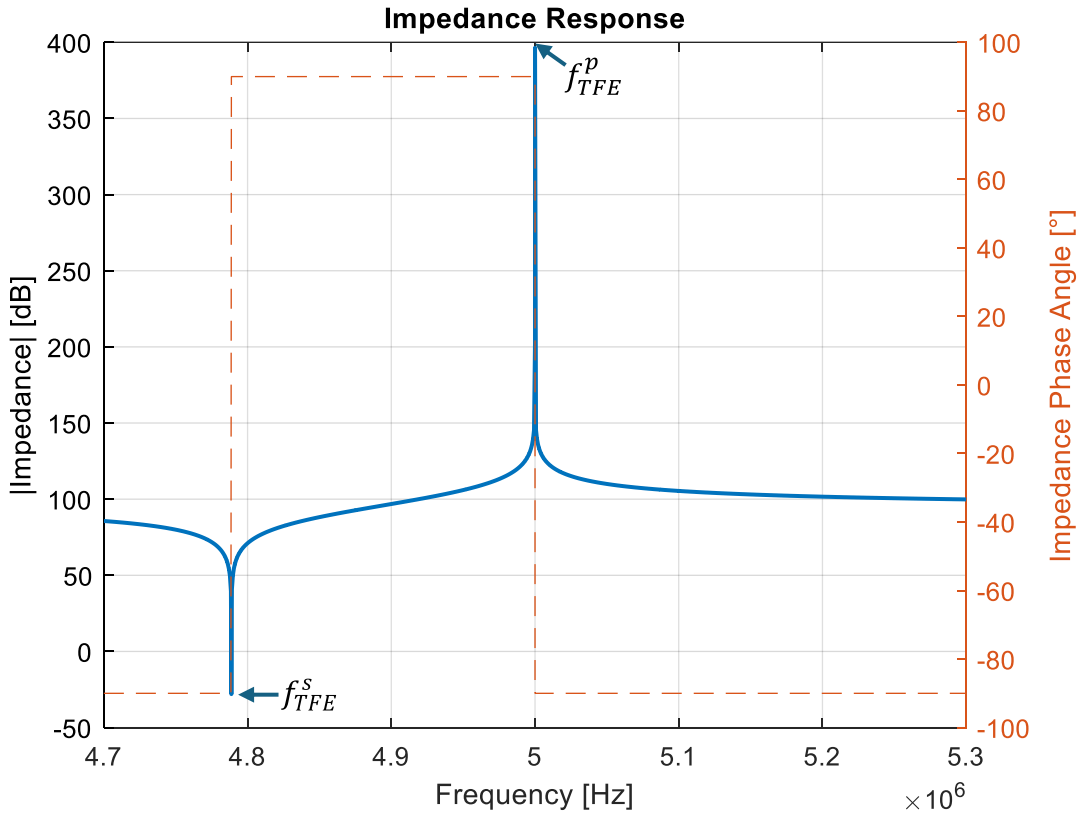

Figure 2-7. Impedance response for idealized TFE resonator.

Similarly, the idealized resonator frequency response in terms of admittance as described by Equation 2.22 is illustrated in Figure 2-8 below.

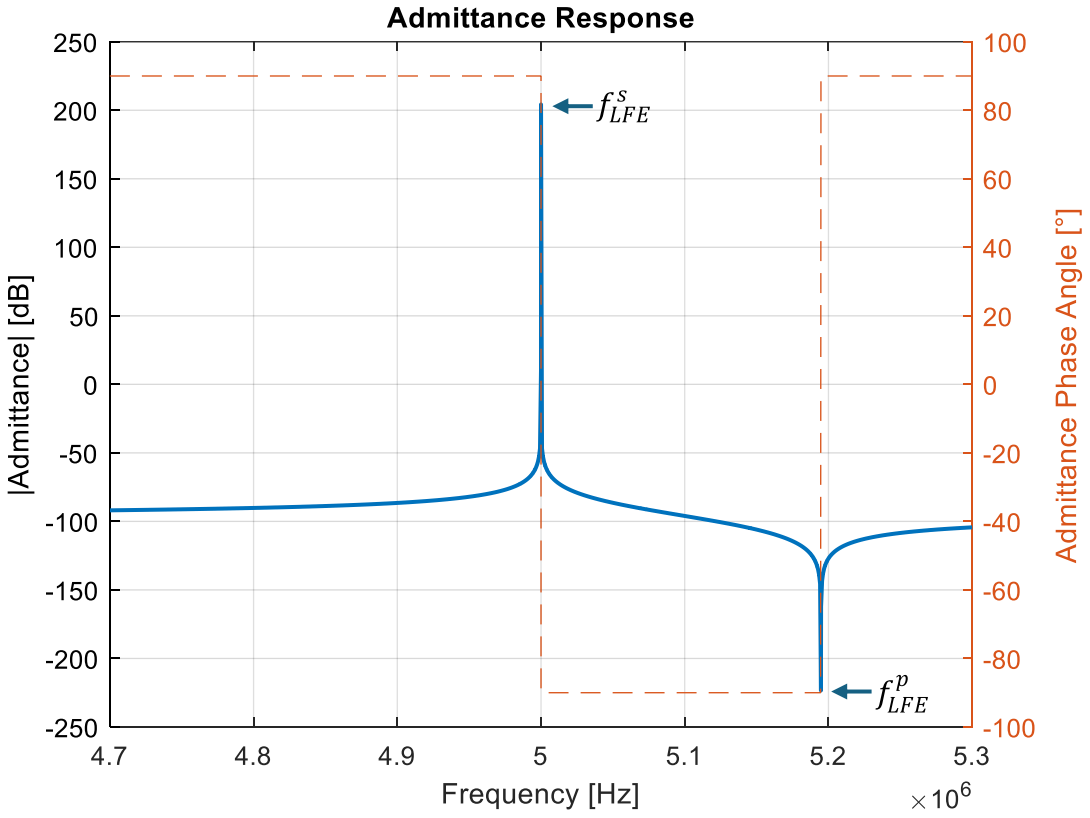

Figure 2-8. Admittance response for idealized LFE resonator.

Figure 2-7 and Figure 2-8 are examples of a single coupled BAW mode, with the phase velocity v^m, electromechanical coupling coefficients $K_{TFE}^{(m)}$ and $K_{LFE}^{(m)}$, as well as C_0^{TFE} and C_0^{LFE} set to be equal in both the TFE and LFE cases. The resonances and anti-resonances for both cases are also marked. The resonance and anti-resonance frequency separation is directly proportional to the electromechanical coupling coefficient. In practice the TFE resonances and anti-resonances normally occur at the two separate instances where the impedance phase angle is zero [7]. This is also normally the case for the LFE admittance response. It should also be

noted that according to Equations 2.20 and 2.21 and Equations 2.23 and 2.24 f_{TFE}^{p} and f_{LFE}^{s} are at the same frequency independent of electromechanical coupling coefficients $K_{TFE}^{(m)}$ and $K_{LFE}^{(m)}$ [1, 14, 16].

2.6 Bulk Acoustic Wave Resonator Temperature Response

The response to temperature variations of BAW modes' electromechanical coupling coefficients, phase velocities, and resonant frequencies can be characterized if the piezoelectric material constants are known as functions of temperature. For example, Smith and Welsh measured the elastic, piezoelectric, and dielectric constants of lithium tantalate (LT) and lithium niobate (LN) in 1971, allowing them to formulate several orders of temperature coefficients for each material constant [4]. These temperature coefficients may be applied to the material constants to describe them as functions of temperature which can be approximated by a Taylor series as follows.

$$c_{xy}(T) = c_{xy}^{0}\left(1 + T_{c_{xy}}^{(1)}(T - T_0) + T_{c_{xy}}^{(2)}(T - T_0)\ldots\right) \tag{2.25}$$

$$e_{xy}(T) = e_{xy}^{0}\left(1 + T_{e_{xy}}^{(1)}(T - T_0) + T_{e_{xy}}^{(2)}(T - T_0)\ldots\right) \tag{2.26}$$

$$\epsilon_{xy}(T) = \epsilon_{xy}^{0}\left(1 + T_{\epsilon_{xy}}^{(1)}(T - T_0) + T_{\epsilon_{xy}}^{(2)}(T - T_0)\ldots\right) \tag{2.27}$$

In the above Equation 2.25 for the elastic constant, Equation 2.26 for the piezoelectric constant, and Equation 2.27 for the dielectric constant, $T_n^{(n)}$ is the nth order temperature coefficient for the given material constant and T_0 is room temperature, 25 °C.

Beyond the material constants, the coefficients of thermal expansion must also be applied to the crystal plate dimensions as follows,

$$h_{xx}(T) = h_{xx}^{0}\left(1 + \alpha_{xx}^{(1)}(T - T_0) + \alpha_{xx}^{(2)}(T - T_0)\ldots\right) \tag{2.28}$$

where h^0 is the initial crystal plate thickness and α_{xx} is the 3x3 matrix for the coefficients of thermal expansion.

Additionally, because the crystal expands and contracts with temperature, while its mass remains constant, its density varies. The crystal plate density must also be modified by the coefficients of thermal expansion as shown below.

$$\rho(T) = \rho^0\left(1 - \left(\alpha_{11}^{(1)} + \alpha_{22}^{(1)} + \alpha_{33}^{(1)}\right)(T - T_0)\ldots\right) \tag{2.29}$$

When temperature variations are under consideration and the material constants become functions of temperature, Equation 2.19 and Equation 2.22 for the immittance responses of a BAW mode also become functions of temperature as shown below.

$$Z_{TFE}(\omega, T) = \frac{1}{j\omega C_0^{TFE}}\left(1 - \sum_{m=1}^{3} {K_{TFE}^{(m)}}^2(T)\frac{tan\left(\frac{\omega}{v_p^{(m)}(T)}h(T)\right)}{\frac{\omega}{v_p^{(m)}(T)}h(T)}\right) \tag{2.30}$$

and

$$Y_{LFE}(\omega,T) = j\omega C_0^{LFE}\left(1+\sum_{m=1}^{3} {K_{LFE}^{(m)}}^2(T)\frac{tan\left(\frac{\omega}{v_p^{(m)}{}_{(T)}}h(T)\right)}{\frac{\omega}{v_p^{(m)}{}_{(T)}}h(T)}\right) \quad (2.31)$$

Finally, to determine the resonance frequency of a BAW mode as a function of temperature, one must first apply the temperature coefficients to their respective rotated material constants at each temperature as described above. Then BAW mode phase velocities and electromechanical coupling coefficients must then be calculated separately at each temperature. Equation 2.30 and Equation 2.31 can then be used to calculate the BAW mode immittance responses at each temperature in order to build the resonance frequency response as a function of temperature.

CHAPTER 3

SIMULATION STUDY

The purpose of the present work is to identify a crystallographic orientation of lithium tantalate which possesses a TSM that is temperature compensated near room temperature. The first step in identifying this cut was to verify the numerical results from previous work [1]. Software was developed with MATLAB to perform the numerical calculations, described in Chapter 2 of this thesis, for bulk acoustic mode phase velocities, electromechanical coupling coefficients, and immittance frequency responses. These calculations were performed for a range of LT orientations at various temperatures. LT material constants and their temperature coefficients from the work of Smith and Welsh [4] were incorporated into these calculations. Simulations were performed for LT crystallographic orientations ranging from (YXwl) 0°/-90° to (YXwl) 0°/90°. Particular attention was paid to the orientation (YXwl) 0°/-84.2°, as this was one of two candidate orientations previously predicted numerically to possess a temperature compensated TSM [1]. Simulations of (YXwl) 0°/-85°, (YXwl) 0°/-86°, (YXwl) 0°/-86.5°, (YXwl) 0°/-87°, and (YXwl) 0°/-90° LT were also emphasized as these were the crystal samples that were able to be purchased from Hangzhou Freqcontrol Electronic Technology LTD. All simulation results were found to be well-aligned with the numerical results from previous work [1].

3.1 Convention for Describing Crystallographic Orientations

The crystal plate orientations of LT involved in this work are described assuming the conventions outlined in the 1987 IEEE Standard on Piezoelectricity [17]. The equations described in Chapter 2 of this thesis assumed that the given acoustic wave of interest propagates in the unprimed coordinate system's x_2 direction. However, in practice, the crystal

plate thickness for a given orientation is not always collinear with the unprimed x_2 direction. Thus, the crystal material constants must be rotated such that in the primed orthogonal coordinate system, x_2 is in the desired propagation direction corresponding to the plate thickness of the given crystal orientation. Figure 3-1 below illustrates the convention for describing crystallographic orientations according to the 1987 IEEE Standard.

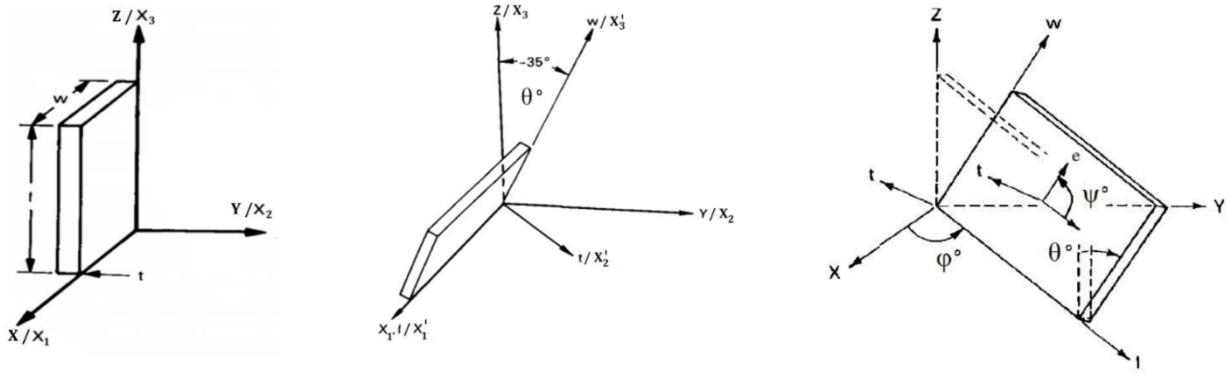

Figure 3-1. (YXwl) 0°/0° (left), (YXwl) 0°/-35° (center), and (YXwl) φ°/θ° (right) crystal plates [1].

To perform the necessary rotations for a given crystal orientation, the crystal plate is first assumed to be oriented in an unprimed orthogonal coordinate system as shown in Figure 3-1 on the left. The width plane, w, is normal to the Z/X_3 direction, the length plane, l, is normal to the X/X_1 direction, and the plate thickness, t, and BAW propagation direction is parallel with the Y/X_2 direction. An example of AT-cut quartz is shown in Figure 3-1 (middle), described by a single rotation about the X axis by -35° in the θ dimension, with 0° in the φ dimension. Finally, in Figure 3-1 on the right a general case is shown with a rotation in each of the three possible dimensions. The third rotation, ψ, simply orients the directions of the laterally exciting electric field and does not affect BAW propagation direction [1]. It does however alter the LFE electromechanical coupling coefficients of the three BAW modes. The crystallographic

orientations of LT that are the focus of this work are singly rotated and can thus be simply described by a single rotation in the θ dimension. (YXwl) 0°/-90° LT, also known as the Z-cut, for example, is oriented by a single rotation about the X axis by -90° in the θ dimension.

3.2 Numerical Calculations

MATLAB was used to generate software which algorithmically performs numerical calculations to simulate the desired LT orientations' behavior at the temperatures of interest. The complete MATLAB script can be found in Appendix A. The first section of code defines constants for room temperature, 25° C, crystal plate capacitance, 1 nF, and a crystal plate thickness of 0.5 mm. Additionally, a frequency vector is defined over which to calculate the immittance frequency response, a temperature vector is defined containing the range of temperatures at which the theoretical LT resonator is to be simulated, and a theta vector is defined containing the rotational values for each of the cuts to be simulated.

In the subsequent section of the MATLAB script, the unrotated material constants, crystal density, elastic constants, piezoelectric constants, and dielectric constants are defined for LT at room temperature according to Smith and Welsh [4]. The respective material constant matrices are then constructed accordingly [4]. After defining the temperature coefficients per Smith and Welsh [4], an iterative loop is entered which indexes through each of the temperature values in the vector previously defined.

3.2.1 Bulk Acoustic Mode Phase Velocities

Within each iteration of the temperature loop the LT material constants are modified by the temperature coefficients as described by Equation 2.25 through Equation 2.29 in Chapter 2

of this thesis. After which, an additional nested loop is entered which indexes through each of the theta rotation values defined in the first section of the MATLAB script. In each iteration of the crystal rotation loop, the appropriate Euler transformation is first executed in order to rotate the material constant matrices [18]. Then the three equations described by Equation 2.15 are constructed, and the three thickness bulk mode phase velocities, v^m, are calculated according to Equation 2.16. Figure 3-2 below shows the simulated phase velocities for each of the three bulk thickness modes for LT cuts (YXwl) 0°/-90° through (YXwl) 0°/90° at room temperature.

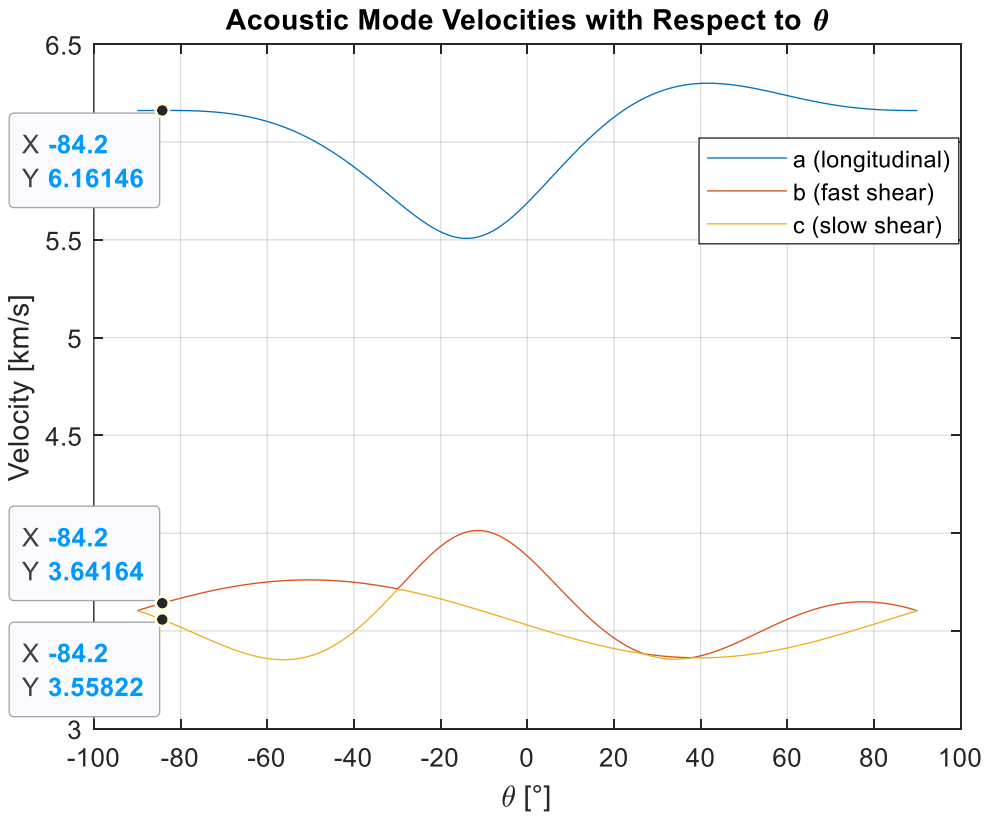

Figure 3-2. $LiTaO_3$ (YXwl) 0°/ θ ° bulk mode phase velocities.

In Figure 3-2 above, markers are placed for the candidate temperature compensated LT cut (YXwl) 0°/-84.2°. It should also be noted that the bulk mode phase velocities are sorted from *a* to *b*, corresponding with the highest phase velocity, always the longitudinal mode, to the lowest phase velocity. The apparent discontinuity shown in Figure 3-2 is simply a result of sorting the phase velocities from highest to lowest, indicating where the two shear modes transition from having the lower phase velocity to having the higher phase velocity and vice versa. The phase velocities of each of the modes are in fact continuous with respect to theta.

3.2.2 Electromechanical Coupling

After the three bulk thickness modes' phase velocities are calculated, the software algorithm computes both the TFE and LFE electromechanical coupling coefficients for each LT orientation as described in Equation 2.17 and Equation 2.18 respectively. Figure 3-3 below shows the simulated TFE coupling for each of the three bulk thickness modes for LT cuts (YXwl) 0°/-90° through (YXwl) 0°/90° at room temperature.

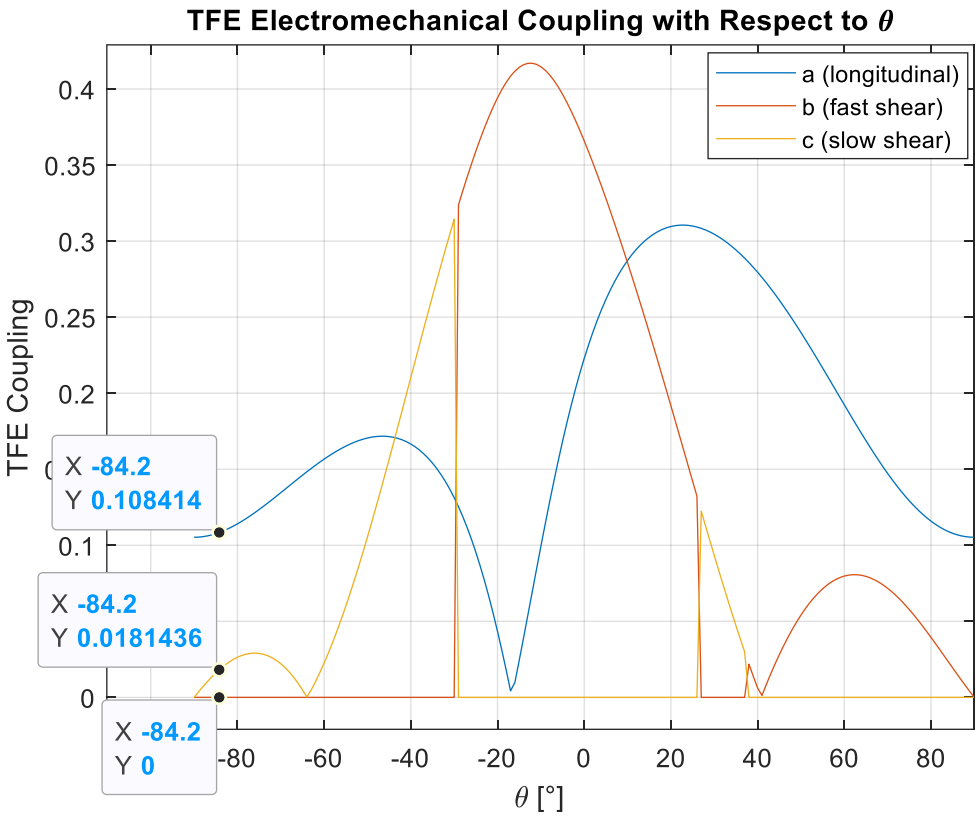

Figure 3-3. $LiTaO_3$ (YXwl) 0°/ θ ° TFE electromechanical coupling.

Similarly, Figure 3-4 shows the LFE coupling for LT cuts (YXwl) 0°/-90° through (YXwl) 0°/90° at room temperature.

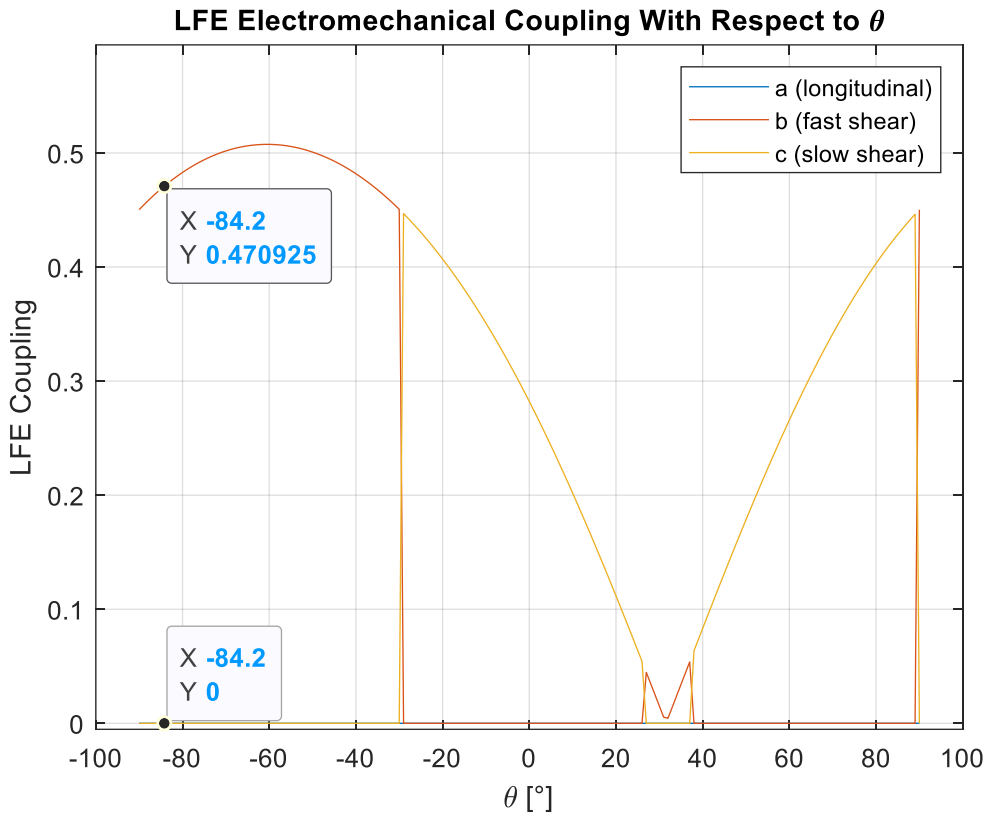

Figure 3-4. $LiTaO_3$ (YXwl) 0°/ θ ° LFE electromechanical coupling.

With the candidate orientation (YXwl) 0°/-84.2° marked on Figure 3-3 and Figure 3-4, several observations can be made. First, in the TFE case, the family of LT orientations which are of interest have higher coupling to the longitudinal mode, relatively low coupling to the slow shear mode and zero coupling to the fast shear mode. Conversely, in Figure 3-4 it can be seen that there is zero coupling to the longitudinal mode and slower of the shear modes, with significantly higher coupling to the faster shear mode. This reinforces the need for the LFE configured LT in order to exploit its higher electromechanical coupling to a temperature compensated TSM. Additionally, it is worth reiterating that the LFE coupling to the LT shear mode shown in Figure 3-4 is nearly seven times higher than that found in LFE AT-cut quartz [1].

3.2.3 Immittance Frequency Response

With the bulk mode phase velocities and electromechanical coupling calculated, the algorithm is then able to proceed with the calculations for the final bulk acoustic mode property examined in this work, the immittance frequency response. Again, these calculations were performed for each of the defined LT orientations, at each of the defined temperature values. Following Equation 2.30, the TFE impedance frequency response was calculated. As an example, Figure 3-5 shows the TFE impedance frequency response for (YXwl) 0°/-84.2° with the series resonance frequency marked.

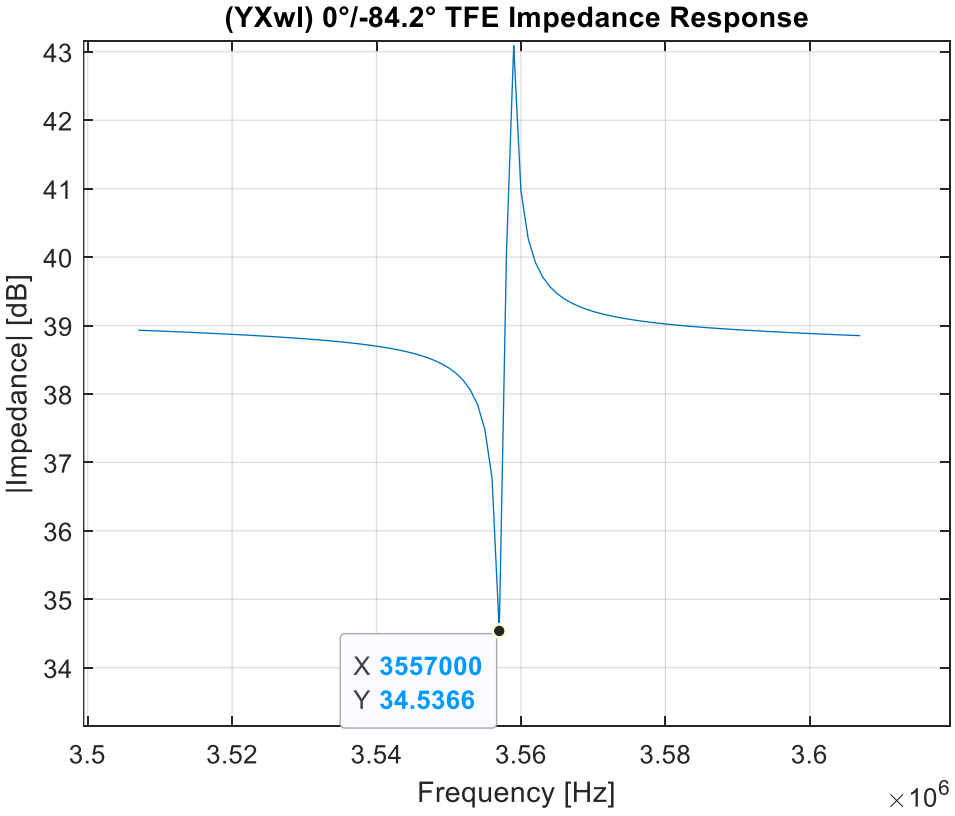

Figure 3-5. $LiTaO_3$ (YXwl) 0°/ -84.2° TFE impedance response.

After the above impedance calculation, the software algorithm implements Equation 2.31 to calculate the LFE admittance frequency response. Again, as an example, the LFE admittance response for (YXwl) 0°/-84.2°, with the series resonance frequency marked, can be seen in Figure 3-6 below.

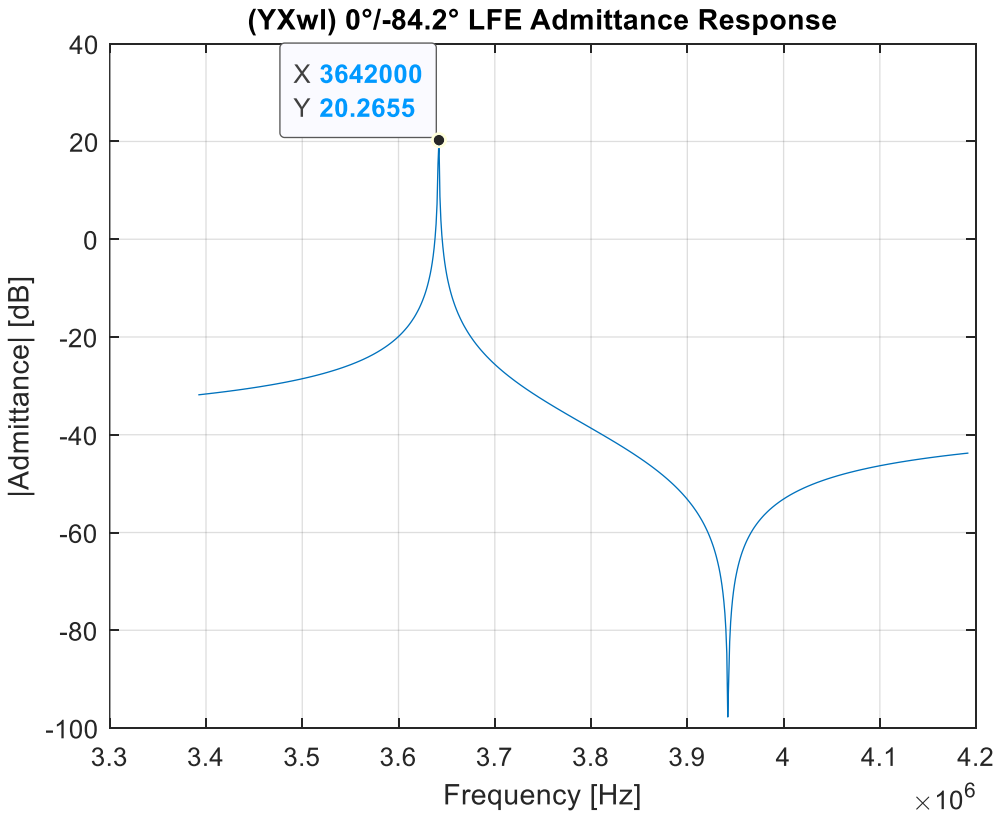

Figure 3-6. $LiTaO_3$ (YXwl) 0°/ -84.2° LFE admittance response.

In Figure 3-5 and Figure 3-6 it can be seen that the frequency span between the series resonance and parallel resonance, or anti-resonance, is much greater in the LFE case. This is correlated with the increased electromechanical coupling in the LFE case, as the electromechanical coupling is directly proportional to the frequency span between the two resonances.

3.2.3 Resonant Frequency Temperature Response

The final task for the simulation software is to characterize each LT orientation's resonance frequency as a function of temperature. Thus far, the software algorithm's process has been described up to the point of having programmatically computed the desired bulk acoustic mode properties for each of the desired LT orientations at each of the temperature setpoints of interest through a series of nested iterative loops. At this stage, the MATLAB script proceeds to identify the precise data points corresponding to the resonance frequencies for each of the LT orientations at each of the temperature setpoints. Because the TFE configuration was determined to not be a feasible option for identifying the temperature compensated, highly coupled TSM, this last computation step was performed only for the LFE case. After compiling the resonance frequency values for each of the LT orientations at each temperature, the software continues to convert these values to a representation of the relative deviation in resonance frequency, as a function of temperature, from the resonance frequency at room temperature. This computation is described by Equation 3.1 below.

$$\Delta f_{LFE}^{S}(T) = \frac{f_{LFE}^{S}(T) - f_{LFE}^{S}(25°C)}{f_{LFE}^{S}(25°C)} \tag{3.1}$$

As shown in Equation 3.1 above, this simple computation takes the resonance frequency at a given temperature, subtracts from it the resonance frequency at room temperature, and normalizes the result by dividing by the room temperature resonance frequency. Additionally, for ease of interpreting the data, the results in the MATLAB script are multiplied by one million for conversion to parts per million (PPM). Figure 3-7 below shows the resulting curve of the

resonance frequency shift as a function of temperature for the LFE (YXwl) 0°/ -84.2° LT orientation.

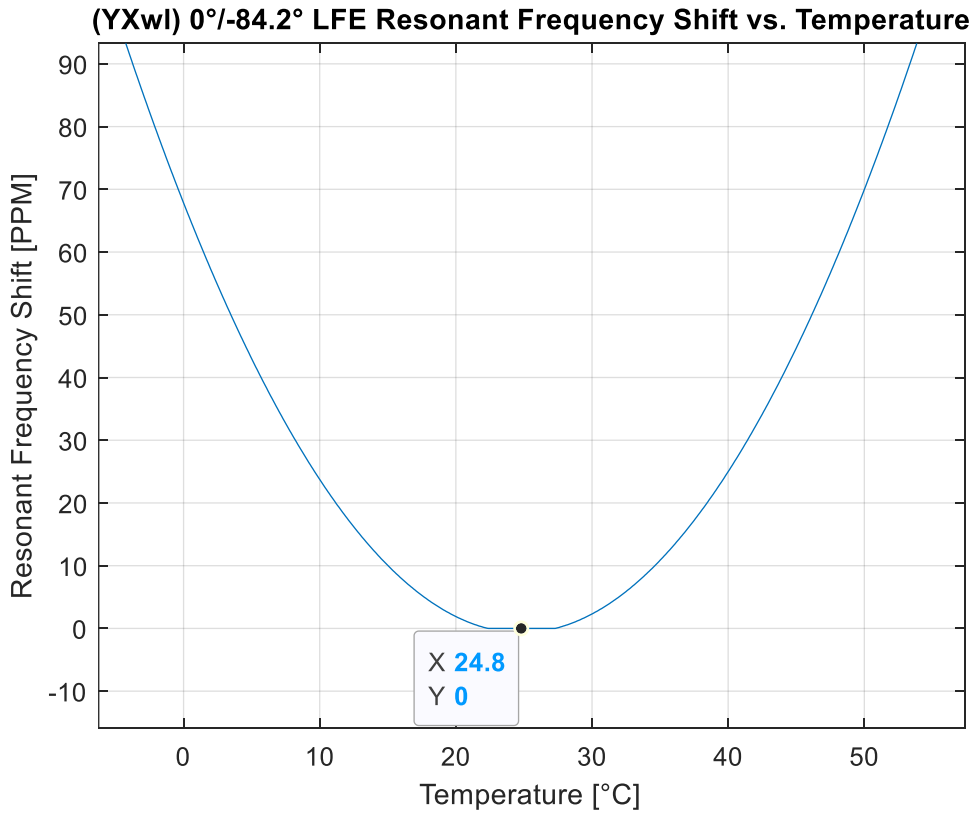

Figure 3-7. $LiTaO_3$ (YXwl) 0°/ -84.2° LFE resonant frequency temperature response.

As shown in Figure 3-7 above, the temperature characteristic of the family of LFE LT orientations of interest is parabolic. The region surrounding the parabolic inflection point is the flattest part of the curve, indicating the greatest temperature stability. This particular LT orientation, (YXwl) 0°/ -84.2°, is numerically predicted to have a temperature response with its inflection point, also known as its turnaround temperature, at precisely 24.8°C, room temperature. A prediction that is corroborated by previous work [1]. It should also be mentioned that the parabolic temperature characteristic of this family of LFE LT orientations

differs from the cubic temperature characteristic of TFE AT-cut quartz (shown in Figure 2-5, Chapter 2), also reflected in the higher order temperature coefficients for quartz. The cubic temperature behavior of TFE AT-cut quartz perhaps does afford more resonance stability over a wider range of temperatures. However, this is possibly offset by the benefits of the LFE configuration described in Chapter 1 and Chapter 2 and the significantly higher LFE electromechanical coupling of LT.

3.2.4 Temperature Coefficient of Frequency

The parabolic temperature behavior of LFE LT is demonstrated in Figure 3-7 and although the turnaround temperature for (YXwl) 0°/ -84.2° LFE LT is room temperature, it varies considerably for other LT orientations. A common identifier for a given orientation's turnaround temperature, which is the inflection point of its temperature response curve, is the first order temperature coefficient of frequency (TCF). The first order TCF is simply defined as the derivative of the resonant frequency shift with respect to temperature, shown in Equation 3.2 below.

$$TCF = \frac{df^S(T)}{dT} \tag{3.2}$$

From here, one can consider a zero-valued TCF at room temperature to be the figure of merit when searching for crystallographic orientations that are temperature compensated. (YXwl) 0°/ -84.2° LT, for example, possesses the zero-valued TCF at room temperature, i.e. the derivative of its parabolic temperature response is zero at its inflection point, or turnaround temperature, which is located at room temperature.

Finally, in addition to (YXwl) 0°/ -84.2°, the resonant frequency shift temperature responses were evaluated for the LT orientations for which physical samples were able to be acquired. The simulated temperatures at which zero-valued TCFs occur for each of these LT orientations is summarized in Table 3-1 below.

Table. 3-1. Simulated turnaround temperatures for various $LiTaO_3$ cuts.

LT Crystallographic Orientation	*Simulated Turnaround Temperature*
(YXwl) 0°/ -84.2°	24.8°C
(YXwl) 0°/ -85°	29.4°C
(YXwl) 0°/ -86°	35.5°C
(YXwl) 0°/ -86.5°	38.6°C
(YXwl) 0°/ -87°	41.9°C
(YXwl) 0°/ -90°	64°C

CHAPTER 4

EXPERIMENTAL VERIFICATION AND RESULTS

4.1 Initial Screening Study

In previous work [1], a theoretical search of all crystallographic orientations of LT identified those exhibiting an LFE TSM with a first order temperature coefficient of frequency (TCF) that is equal to zero at room temperature. The TSM's first order TCF is defined as the derivative of its series resonance frequency with respect to temperature. To experimentally study these temperature compensated cuts, LT samples ranging in orientations from (YXwl) 0°/-85° to (YXwl) 0°/-90° (Z-cut) were acquired and tested.

For initial experimental screening, two pairs of Z-cut plano-plano LT samples were first obtained from two different manufacturers. The first pair was purchased from Yamaju Ceramics Co. LTD, the same source used in previous research [1]. The second pair was purchased from Hangzhou Freqcontrol Electronic Technology LTD. All samples were approximately 2 inches in diameter and 0.5 mm in thickness. As shown in Figure 4-1, each pair contained what is known as a black LT sample and a white LT sample.

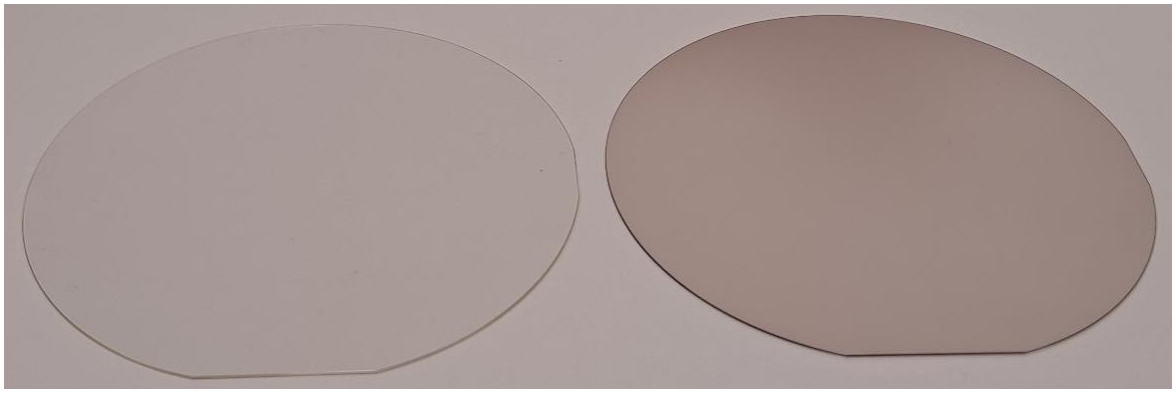

Figure 4-1. White (left) and black (right) $LiTaO_3$ samples.

Black LT is LT that has been treated for suppression of pyroelectricity, a process known as "blackening," while white LT is left untreated. The purpose of this initial study was three-fold: to verify previous experimental results for (YXwl) 0°/-90° LT, confirm the understanding that to be useful LT must necessarily be blackened to suppress pyroelectric effects, and to compare crystal quality between two different manufacturers.

4.1.1 Sample Preparation

The black and white LT wafers were first confirmed to be of the correct Z-cut orientation using X-Ray Diffraction (XRD) techniques. They were then diced into samples of manageable size and shape, squares of 0.55-inch sides, as shown in Figure 4-2 below.

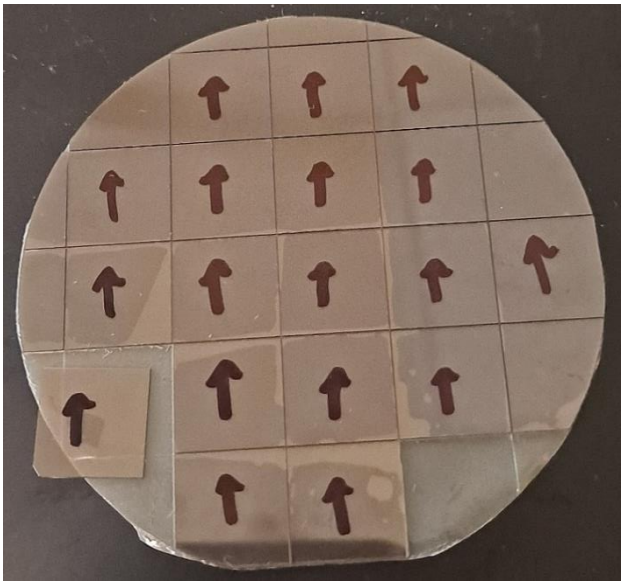

Figure 4-2. Black $LiTaO_3$ wafer, diced into individual samples.

After dicing, each sample was then cleaned with acetone, methanol, isopropanol, and deionized water in sequential fashion. While handling the samples, care was taken to keep track of their rotational orientation with respect to the major flat of the original wafer, which can be

seen in Figure 4-1 and Figure 4-2. The arrows shown in Figure 4-2 were marked on each sample accordingly.

4.1.2 Baseline Measurements

Following their preparation, baseline measurements were taken manually for each of the black and white LT samples. An Agilent E5071C ENA Vector Network Analyzer (VNA) and an LFE test fixture, constructed on a printed circuit board (PCB), were used to obtain scattering parameter (S-parameter) data for each sample. Figure 4-3 shows the setup for baseline measurements.

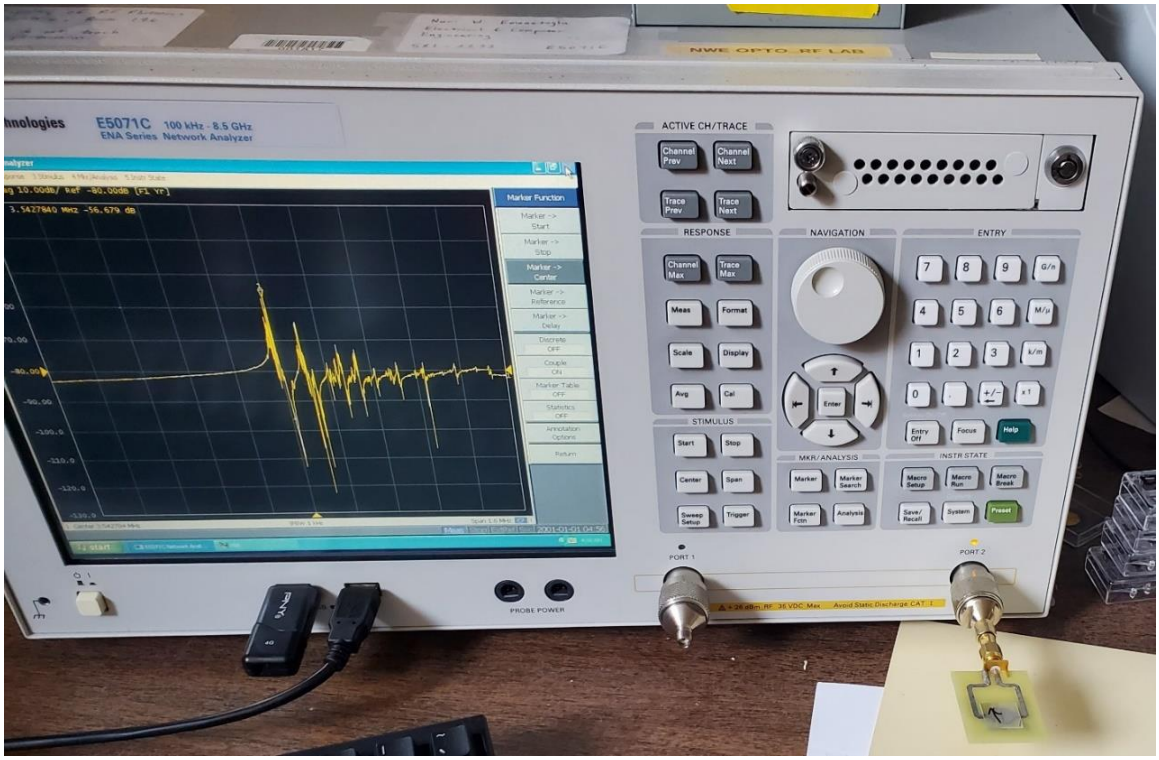

Figure 4-3. VNA and PCB test fixture used to acquire baseline measurements.

The fundamental resonances of each of the samples at room temperature were assessed by analyzing their frequency responses in terms of admittance magnitude. The

fundamental resonance frequency for each sample was found to be between 3.5 MHz and 3.6 MHz, confirming the numerical expectation based on simulation data for a Z-cut LT crystal plate with a thickness of 0.5 mm.

The VNA was calibrated according to the expected resonant frequency of 3.6 MHz. Pure shear resonances were measured primarily in four different ways. First, a wide measurement was taken, with a 1.6 MHz frequency span and an intermediate frequency bandwidth (IFBW) of 1 kHz. To examine finer resonance characteristics including spuriousness and precise magnitudes, a second narrow measurement was taken with a 48 kHz frequency span and a 30 Hz IFBW. These resonance measurements were repeated for each LT sample using three different PCB test fixtures with varying LFE electrode configurations. The PCB's electrode patterns were all 0.9 mm in diameter, with electrode gaps of 0.5 mm, 1.5 mm, and 2.5 mm. No appreciable differences in the samples' responses for each electrode pattern could be observed. It is possible that an abundance of spurious modes obscured the effects of the different electrodes. Nevertheless, because smaller electrode gaps result in higher electric field strength, and it has been shown that LFE sensors have increased sensitivity with smaller electrode gaps [2], the 0.5 mm electrode gap configuration was selected as a suitable standard for further measurements.

Tests were also performed to assess the degree to which the arrows marked on each sample contributed to mechanical loading, and subsequent shifts in the crystal's resonant frequency. In comparing the responses of several samples, marked and unmarked, it was determined that no significant resonant frequency shifts could be observed. Finally, a brief harmonic analysis was carried out for several of the samples. Among the samples tested,

resonances were measured reliably up to the 41st harmonic, at roughly 145 MHz. With higher quality, thinner cut samples, and a more thorough study, it is likely that much higher harmonic resonances could be observed [3].

The S-parameter data collected from baseline measurements was parsed and analyzed using MATLAB software. The fundamental shear resonances of the black and white sets of LT samples were compared in order to identify the samples with the strongest, least spurious admittance responses. The samples determined to have the highest quality responses in each set were selected for use in the temperature characterization process.

4.1.3 Temperature Response Measurements

The temperature responses of several of the highest quality LT samples were tested using the same VNA and PCB test fixture as described in the previous section. In this case, the samples and PCB were placed inside a proportional integral derivative (PID) controlled Tenney environmental test chamber (ETC), with a resistance temperature detector (RTD) measuring local temperature. The VNA outside the chamber obtained port parameter data for each sample through standard 50 Ω coaxial cables connected to the test fixture. A PC running MATLAB® swept the temperature in ETC, recorded the fixture temperature and acquired data from the VNA. The test setup can be seen in Figure 4-4 below.

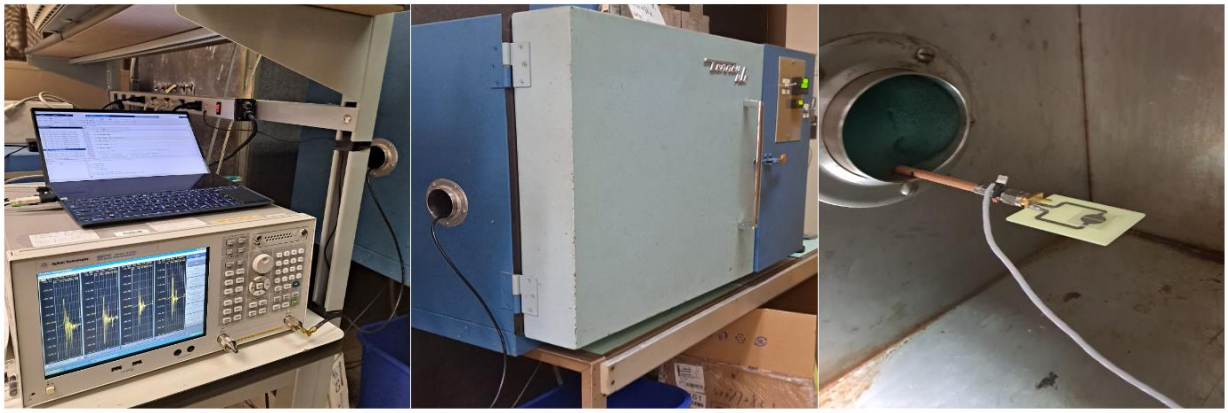

Figure 4-4. Temperature response measurement setup.

Initial tests were performed by selecting setpoints on the PID controller and ramping the temperature in the chamber by 10 °C increments manually. The VNA output was visually assessed to determine whether the LT sample under test had reached thermal equilibrium. S-parameter data was then captured manually after roughly 15-minute soak times at each temperature setpoint. Analysis of the resulting data did not find the expected behavior of the LT samples and indicated that, to adequately explore the LT's temperature behavior, a more systematic approach capturing more resonance data at finer temperature increments and longer soak times was required. Moreover, spuriousness and noise made tracking the shifting resonance peak of the fundamental difficult to do when analyzing the temperature response data. As such, the 5^{th}, 7^{th}, 9^{th}, and 11^{th} harmonics, which appeared to exhibit less coupling to spurious modes, were chosen to be tracked simultaneously. The continued redesign and increasing complexity of the measurement process became such that it could not be carried out manually. Consequently, an automated process of measurement was developed. A MATLAB script was formulated, through iterative trial and error, so that a PC could remotely operate both the ETC and VNA via RS-232C and USB serial interfaces, respectively. The MATLAB script

can be found in Appendix B. This provided programmable control of the PID's temperature ramping functions on the ETC. It also allowed for automatic acquisition of temperature measurements from the RTD, and control of the VNA for the capture of LT resonance data. This setup can be seen in Figure 4-4.

In the final design of the measurement process the ETC was programmed to ramp its internal temperature from roughly 25 °C to 90 °C in setpoint increments of 5 °C. A temperature soak of 90 minutes was implemented at each setpoint to allow the LT samples to fully stabilize to thermal equilibrium. The VNA was programmed to take a resonance measurement of each harmonic every 30 seconds, beginning after the first 45 minutes of the 90-minute temperature soak. The data from each VNA measurement, along with temperature measurements from the ETC, were synchronously collected and saved to the PC. Following the completion of a temperature test, the collected data was parsed and analyzed in MATLAB for the characterization of the LT's temperature response behavior.

4.1.4 Initial Screening Study Results

Following the collection of resonant frequency data, plots of the data, along with 2nd order fits, were generated for analysis and comparison with the results of previous research [1]. The data was portrayed in terms of the deviation in resonant frequency, as a function of temperature, from the resonant frequency at room temperature. This can be expressed as $\Delta f/f(25°C)$, in parts per million (PPM).

4.1.4.1 White LiTaO3

The temperature response data for the white LT samples is shown in Figure 4-5 below.

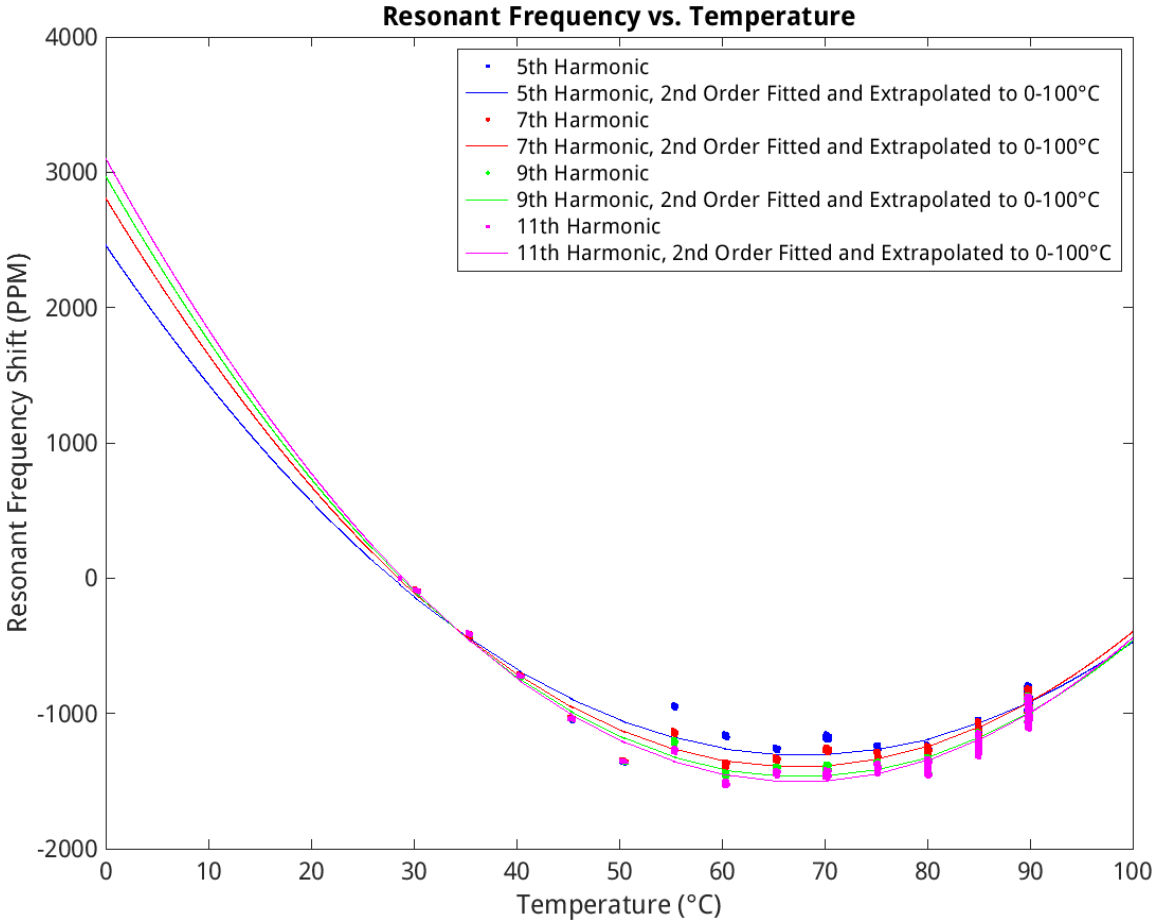

Figure 4-5. White $LiTaO_3$ temperature response data.

Data for the white LT was collected at temperatures roughly from room temperature to 90 °C. 2nd order fits to the data were applied and extrapolated to the range of 0 °C to 100 °C. A clear parabolic trend can be seen, with an inflection point around 70 °C, yet the variations in resonant frequency are considerably large in magnitude. Additionally, as also cited in previous work [1], sporadic frequency drifts from both white LT samples were observed at higher temperatures. In Figure 4-5, especially large positive shifts can be observed after about 55 °C.

This behavior may be related to the pyroelectric properties of the untreated white LT, causing an accumulation of charge in the material until spontaneous polarization occurs around 55 °C. More work is required however to accurately describe this behavior and ascertain the extent to which pyroelectricity is responsible. Currently, the instability of the white LT samples likely precludes any practical benefit to be exploited from their temperature behavior.

4.1.4.2 Black $LiTaO_3$

The data collected from testing the temperature behavior of the black LT samples from both manufacturers correlates well with prior findings, with both samples exhibiting a zero TCF inflection temperature at about 50.5 °C. Data for all harmonic resonances tracked from room temperature to 90 °C is shown, with 2nd order fits in Figure 4-6 below.

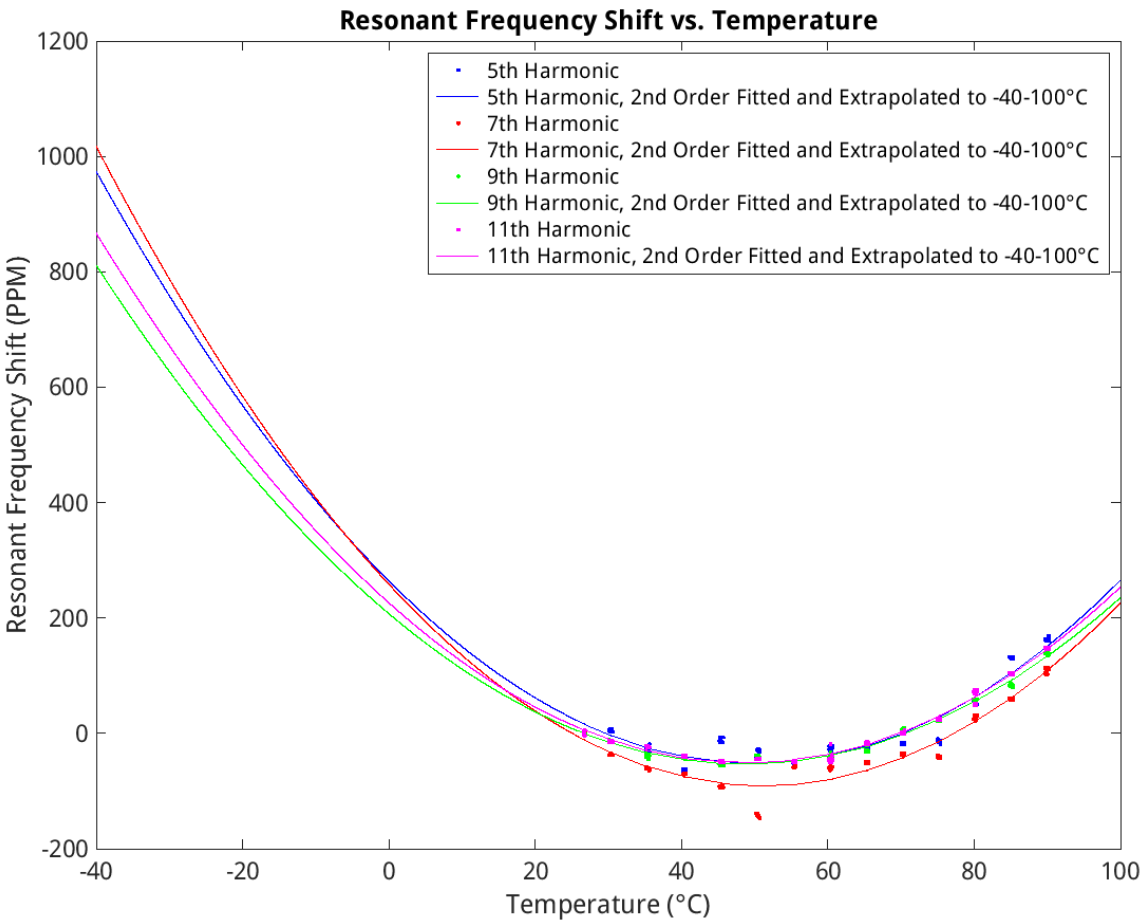

Figure 4-6. Black $LiTaO_3$ temperature response data.

The magnitudes of frequency shifts can be seen to be notably low when compared with those in the white LT. Furthermore, Figure 4-7 and Figure 4-8 illustrate the extent to which the pyroelectrically suppressed black LT possesses temperature stable shear resonances in comparison with the untreated white LT.

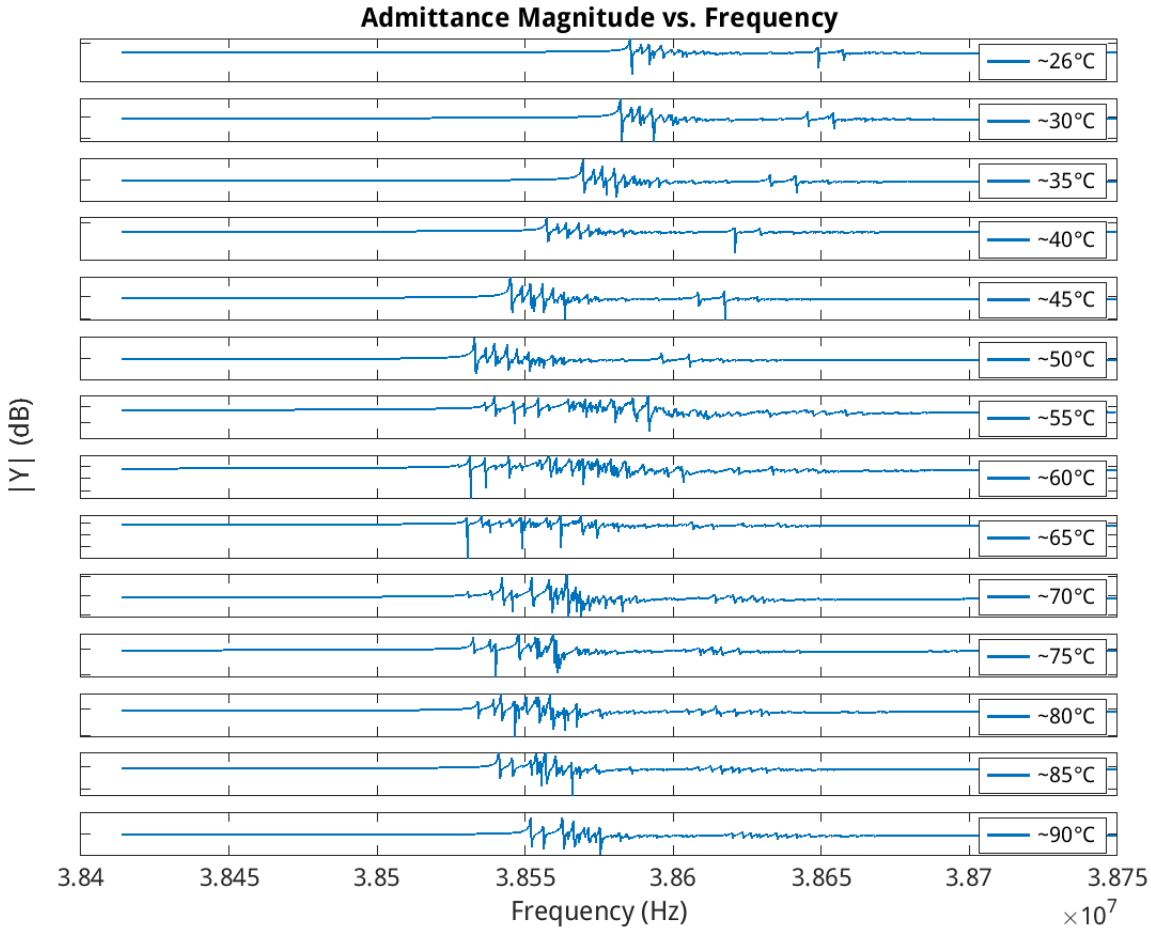

Figure 4-7. White $LiTaO_3$ resonances at different temperatures.

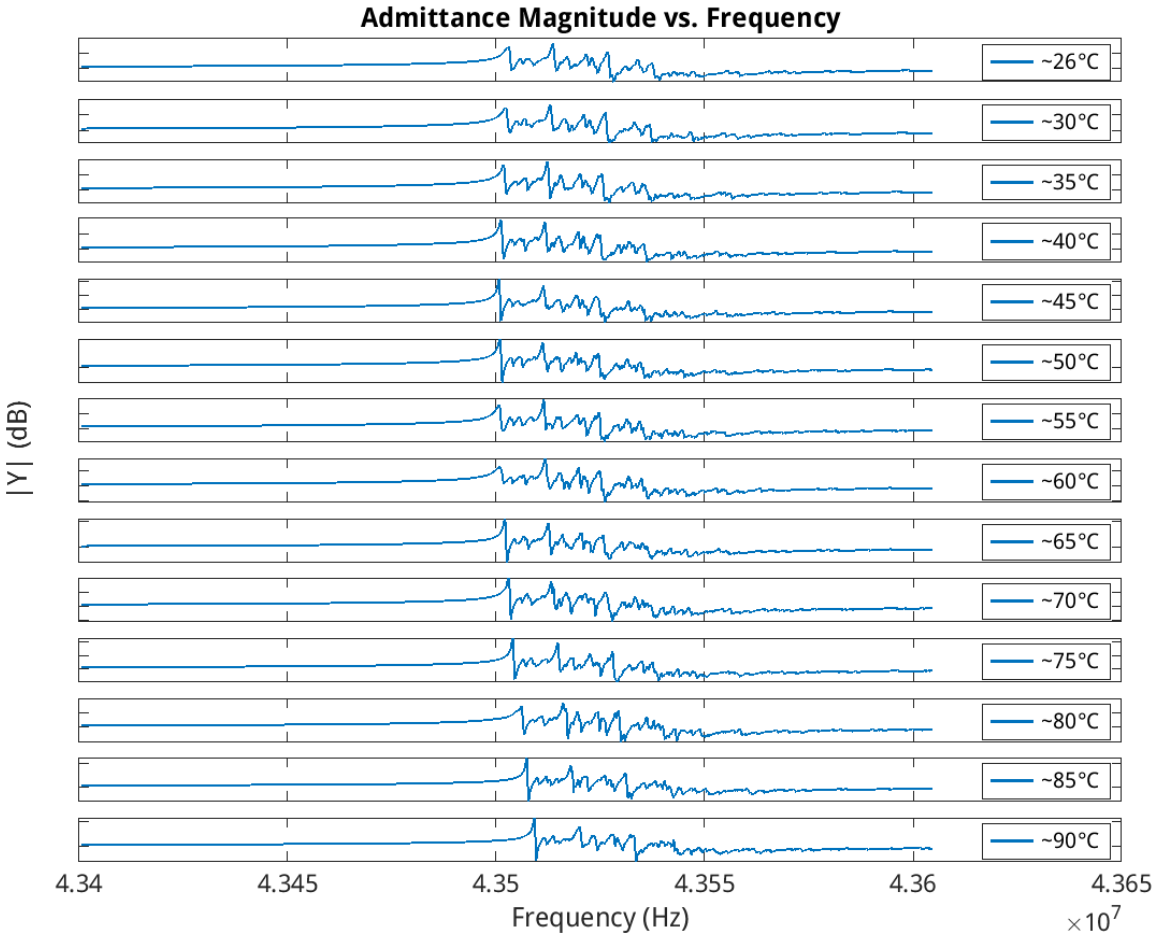

Figure 4-8. Black $LiTaO_3$ resonances at different temperatures.

The resonant frequency of the white LT can be seen in Figure 4-5 and Figure 4-7 to experience much greater, sporadic shifts, on the order of thousands of PPM, with substantially more energy loss to spurious modes. In contrast, the resonance of the black LT in Figure 4-6 and Figure 4-8 is much more stable and non-spurious across varying temperatures, exhibiting shifts on the order of tens to hundreds of PPM.

4.2 Experimental Verification of Temperature Compensated $LiTaO_3$

To narrow in on the room temperature compensated cut, additional black LT samples of the orientations (YXwl) 0°/-85°, 0°/-86°, 0°/-86.5°, 0°/-87°, and 0°/-90° were purchased from the more affordable Hangzhou Freqcontrol Electronic Technology LTD. These plano-plano 0.55-inch diameter circular samples were 0.5 mm thick. Room temperature baseline measurements were again taken to assess the frequency responses of each of the samples. The same VNA and LFE test fixture, with 0.9 mm diameter, 0.5 mm gapped electrodes, were used to obtain S-parameter data for each sample. The fundamental resonances, as well as up to the 13th harmonics, of each of the samples were assessed by analyzing their frequency response in terms of admittance magnitude. The fundamental frequency for each sample was again found to be between 3.5 MHz and 3.6 MHz, corroborating previous simulation data. The fundamental resonances were first located using a wide span of 1.6MHz on the VNA, then were examined qualitatively at a narrower span of 48 kHz. It can be seen in Figure 4-9 that, similarly to the previous diced square samples, the fundamental resonances of these samples were plagued by significant coupling to spurious modes. This is likely due to the poor energy trapping associated with the plano-plano geometry of the samples. This spuriousness caused shifts in the fundamental frequency to be difficult to differentiate and track across wide temperature ranges. However, as also demonstrated in Figure 4-9, the higher order harmonics tended to be much cleaner and less spurious. For this reason, higher order harmonics up to the 13^{th} were tracked within a narrower span of 16kHz during temperature tests on the samples.

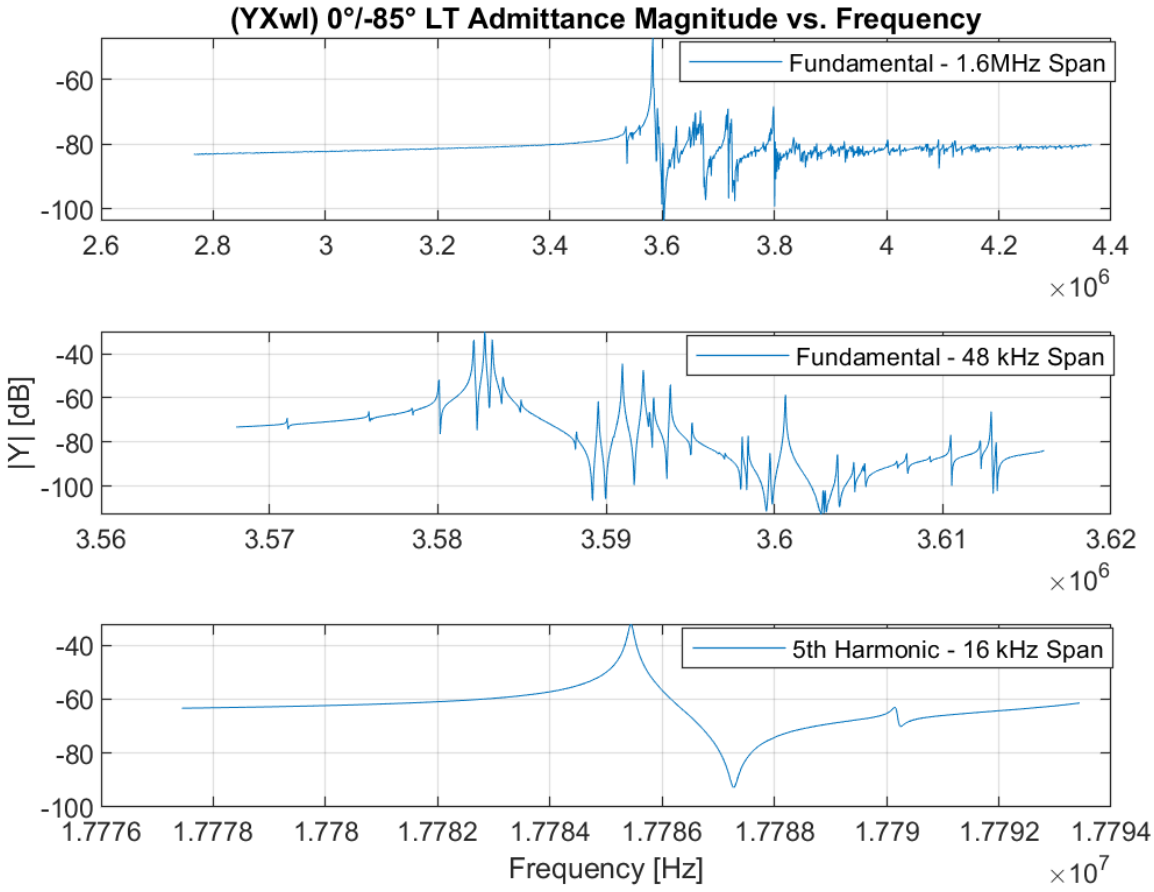

Figure 4-9. (YXwl) 0°/-85° $LiTaO_3$ sample's fundamental resonance and fifth harmonic.

The temperature responses of each of the LT samples were tested using the same setup previously described, with the VNA, LFE test fixture, ETC, and RTD, all controlled by a PC running a MATLAB script.

4.2.1 Experimental Results

The curves in Figure 4-10 below were generated from S-parameter data for each LT sample's ninth harmonic.

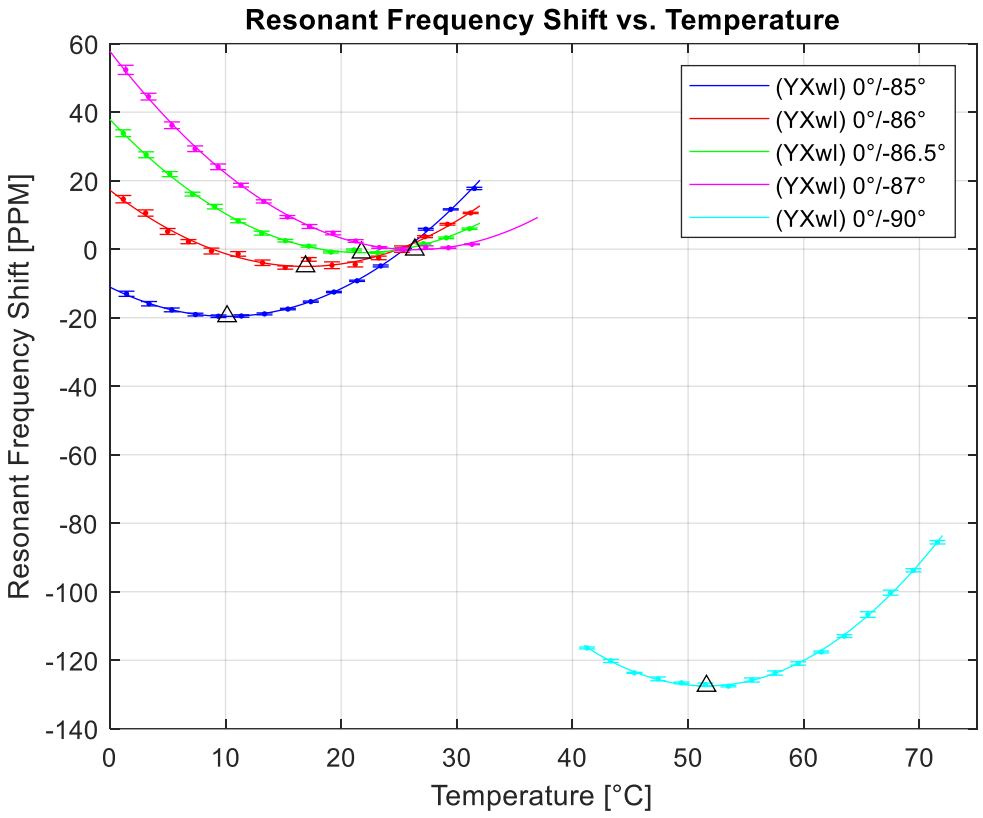

Figure 4-10. Temperature responses of $LiTaO_3$ samples' 9th harmonics.

The triangles in Figure 4-10 mark the inflection point of the second order fitted parabolic curves, which also coincides with the temperature at which the derivative of the resonant frequency with respect to temperature is equal to zero. The data points Figure 4-10 correspond with the average temperature values of 55 measurements taken at each temperature setpoint. The temperature response of the (YXwl) 0°/-90° sample matches the previous experimental

results for the same cut with a zero TCF in the vicinity of 50°C. However, the temperature responses of all samples deviate from theoretical predictions as summarized in Table 4-1 below.

Table 4-1. Simulated versus measured turnaround temperatures for each $LiTaO_3$ cut.

Crystallographic Orientation	*Simulated Turnaround Temperature*	*Measured Turnaround Temperature*	*Error*
(YXwl) 0°/ -85°	29.4°C	10.1°C	65.6%
(YXwl) 0°/ -86°	35.5°C	16.9°C	52.4%
(YXwl) 0°/ -86.5°	38.6°C	21.7°C	43.8%
(YXwl) 0°/ -87°	41.9°C	26.4°C	37%
(YXwl) 0°/ -90°	64°C	51.6°C	19.3%

Similar deviations to those shown in Table 4-1 were also found between the simulated and experimental results of previous work, with the predicted temperature compensated (YXwl) 0°/-84.2° cut experimentally exhibiting at turnaround temperature of 2.5°C, a 90% error from the predicted 25°C [1]. Because the present work's numerical results corroborate those of previous work, as discussed in Section 3.2, it is thought that the possible reason for the deviation is the same for both studies. Namely, the quality of contemporary grown LT crystals is likely to be different than those grown in the 1970s, when Smith and Welsh documented the LT material constants and temperature coefficients [4]. In any case, it can be seen in Table 4-1 that the zero TCF for the (YXwl) 0°/-87° sample is located at about 26.4°C, making this the room temperature compensated LT cut that has been sought. Furthermore, in Figure 4-11 below is the temperature response of the (YXwl) 0°/-87° cut shown in more detail with the second order

fit extrapolated to 37 °C, where it can be seen to exhibit frequency shifts of less than 10 PPM at 10 °C above or below its inflection point.

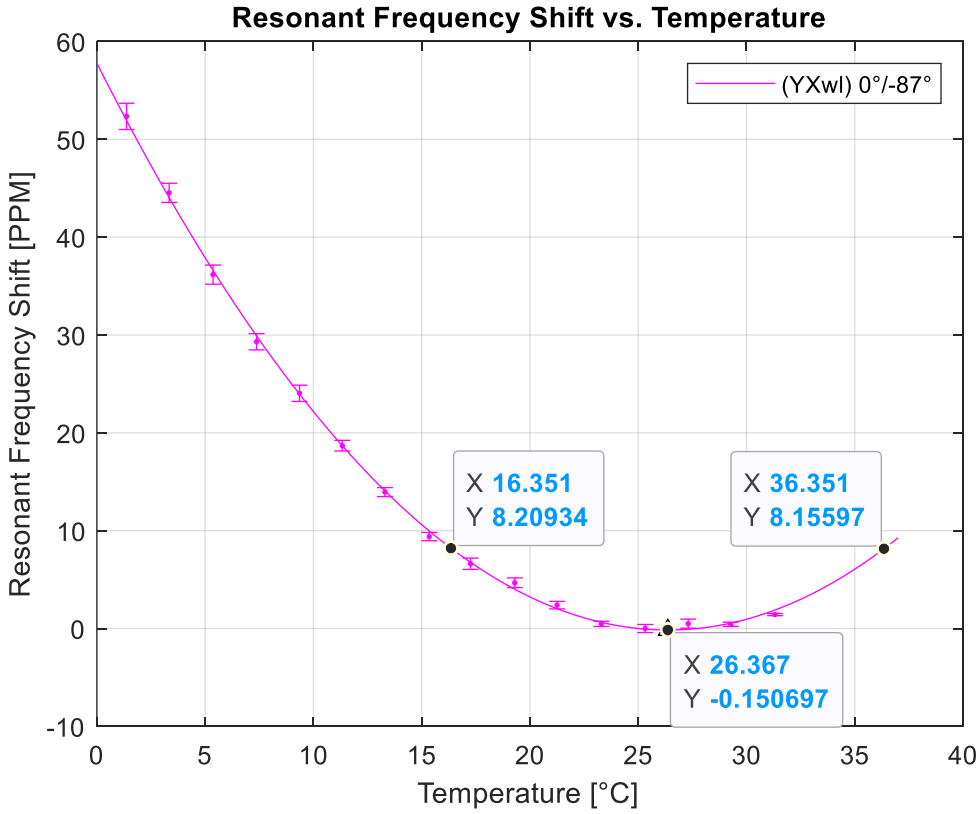

Figure 4-11. Temperature response of (YXwl) 0°/-87° $LiTaO_3$ sample's 9th harmonic.

The temperature stability of the (YXwl) 0°/-87° LT cut shown in Figure 4-11 is still inferior to that of AT-cut quartz, with 10 PPM of frequency shift at plus or minus 50 °C, shown in Figure 2-5. However, the moderate temperature stability may still provide utility when considered in conjunction with LT's high electromechanical coupling.

Finally, Figure 4-12 below shows that there is a roughly linear relationship between LT crystal cut angle and temperature inflection point/turnaround temperature.

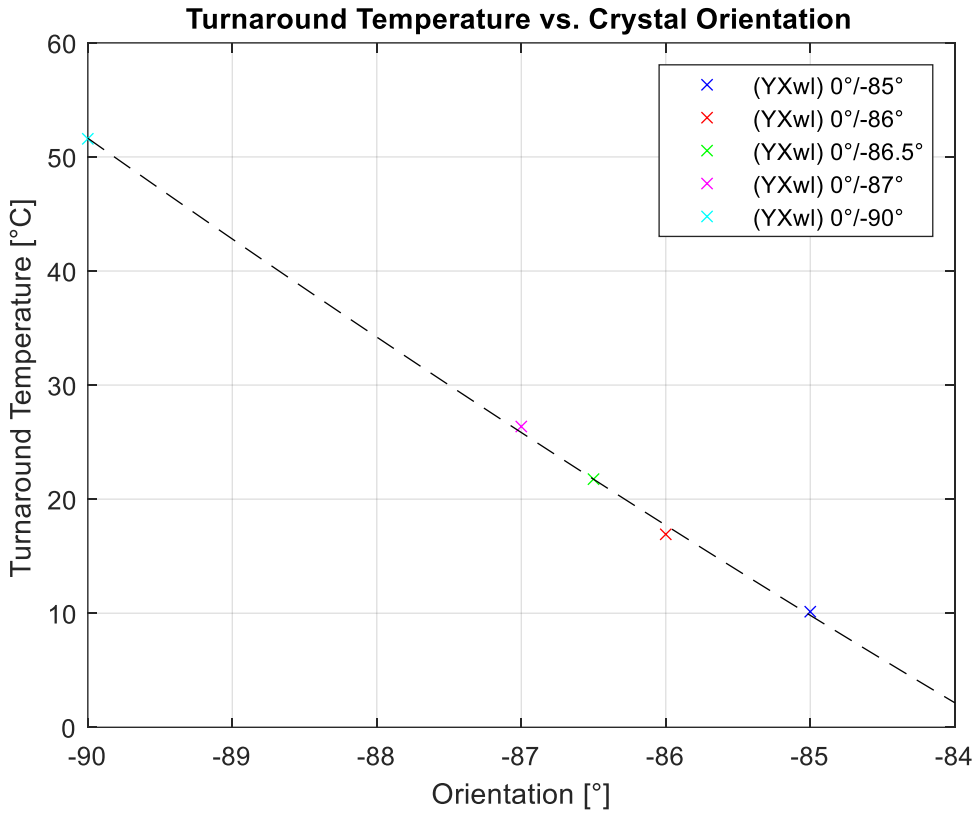

Figure 4-12. Turnaround temperature versus $LiTaO_3$ crystallographic theta orientation.

The linear relationship between turnaround temperature and crystallographic orientation shown in Figure 4-12 implies that the temperature at which the zero-valued TCF occurs could be adjusted with relative ease by modifying the LT crystal orientation.

CHAPTER 5

CONCLUSIONS AND FUTURE WORK

5.1 Conclusions

A room temperature compensated lithium tantalate orientation, (YXwl) 0°/−87°, was experimentally demonstrated in this work. Theoretical calculations were performed to identify the temperature compensated orientation which, as discussed in Section 3.2, matched previously reported theoretical predictions. A comparative study between LT samples from two different vendors led to the conclusion that they were of equivalent quality. A series of blackened LT samples of the orientations (YXwl) 0°/−85°, (YXwl) 0°/−86°, (YXwl) 0°/−86.5°, (YXwl) 0°/−87°, and (YXwl) 0°/−90° were acquired from Hangzhou Freqcontrol Electronic Technology LTD. The (YXwl) 0°/−87° sample had a zero valued temperature coefficient of frequency at 26.4°C, closest to room temperature. Temperatures at which each of the six purchased samples exhibited a zero TCF were demonstrated to trend roughly linearly with crystal orientation, from about 10.1°C for (YXwl) 0°/−85° to about 51.6°C (YXwl) 0°/−90°.

The theoretical search for a temperature compensated cut was accomplished by computing several of the bulk acoustic wave parameters for a range of LT orientations across varying temperatures. In order to compute these bulk acoustic wave parameters, LT material constants and temperature coefficients were taken from the Smith and Welsh dataset [4] and applied to the coupled acoustic and electromagnetic wave propagation equations using the quasi-static approach. Using software developed with MATLAB, the bulk acoustic mode resonance frequencies, phase velocities, thickness field excitation coupling coefficients, lateral field excitation coupling coefficients, and 1st order temperature coefficients of frequency were

computed as functions of temperature and crystallographic orientation. These numerical results were found to be consistent with previous work by Jason McGann [1], which had predicted two temperature compensated orientations of LT which have pure shear modes with zero-valued TCFs at room temperature, (YXwl) 0°/−16.4° and (YXwl) 0°/−84.2°.

At the onset of the experimental portion of this work, a screening study was executed using two sets of Z-cut (YXwl) 0°/−90° samples of LT. One set was purchased from Yamaju Ceramics Co. LTD, and the other was purchased from Hangzhou Freqcontrol Electronic Technology LTD. Each set of samples contained an untreated, white LT wafer and a black LT wafer, treated for suppression of pyroelectricity. The intentions for these samples were to reinforce the validity of numerical results for this cut of LT, replicate previous experimental results, validate the difference between white LT and black LT, and compare the quality of the crystals from two different manufacturers. The results of these studies were consistent with previous experimental work but deviated from theoretical predictions using the material constants presented by Smith and Welsh in 1971. This deviation, summarized in Table 4-1, can be accounted for by the differences in crystal quality between the current samples and those grown in the 1970s. The samples purchased from two different manufacturers were found to perform comparably. Finally, the initial screening study led to the determination that pyroelectric effects in white LT increased noise in the frequency response, and caused large frequency shifts, which made tracking resonances across varying temperature responses difficult and impractical. Thus, it was determined that blackened LT must be used for viable devices.

The next phase of experimental work was focused on narrowing in on the LT orientation possessing a temperature compensated pure shear mode at room temperature. For this purpose, additional samples of blackened LT ranging in orientation from (YXwl) 0°/−85° to (YXwl) 0°/−90° were purchased from Hangzhou Freqcontrol Electronic Technology LTD. Although the current numerical models had predicted the sought-after temperature compensated cut to be (YXwl) 0°/−84.2° this was not found to be case experimentally, with this cut exhibiting at turnaround temperature of 2.5°C, as discussed in Section 4. Linear interpolation was performed to modify the prediction for the temperature compensated orientation to be at (YXwl) 0°/−86.8° [1]. Experimental characterization of each of the purchased samples' resonance frequencies at a range of temperatures found the (YXwl) 0°/−87° sample to have a zero valued TCF at 26.4°C, the closest to room temperature. Furthermore, the temperatures at which each of the five purchased samples exhibited a zero TCF were demonstrated to trend roughly linearly with crystal orientation. These resulted were presented at the 2023 IEEE International Ultrasonics Symposium in Montreal, Canada, and published [5].

5.2 Future Work

Theoretical calculations using the Smith and Welsh dataset from 1971 predicted the LT cut that is temperature compensated at room temperature to be (YXwl) 0°/−84.2° while this work experimentally demonstrated the correct orientation to be closer to (YXwl) 0°/−87°. Thus, there is a need to either confirm or re-characterize the material constants of LT crystals grown using modern fabrication techniques, including their temperature coefficients. The LT crystals grown currently are presumably higher in quality than those grown at the time of the initial characterization that resulted in the documentation of LT material constants. As such, an

opportunity exists to possibly improve the characterization and definition of LT material constants to be more in line with experimental results.

Additionally, theoretical calculations have identified a second candidate orientation of LT, (YXwl) 0°/−16.4°, which may possess a temperature compensated pure TSM [1]. This LT orientation should be pursued and characterized experimentally.

Methods for strengthening the resonant response of lateral field excited LT resonators should be explored, including increasing the Q-factor and reducing the coupling to spurious modes. These techniques include electrode deposition, crystal surface contouring, or bonding with other substrates. Ultimately, the aim of this research is to result in the production of a bulk acoustic wave sensing platform of lateral field excited LT for use in high sensitivity liquid-phase applications, particularly biosensing. Future work focusing on the development of an LT sensing platform could profoundly impact sensor systems in agriculture, homeland security, global warming, and medical applications.

REFERENCES

[1] McGann, Jason M., ”Piezoelectric Platforms for Bulk Acoustic Wave Sensor Applications” (2017). Electronic Theses and Dissertations. 2682. https://digitalcommons.library.umaine.edu/etd/2682

[2] Y. Hu, L. A. French, K. Radecsky, M. P. Da Cunha, P. Millard, and J. F. Vetelino, IEEE Trans. Ultrason. Ferroelectr. Freq. Control 51, 1373 (2004).

[3] D. F. Mccann, J. M. Mcgann, J. M. Parks, D. J. Frankel, M. P. Da Cunha and J. F. Vetelino, ”A lateral-field-excited LiTaO3 high-frequency bulk acoustic wave sensor,” in IEEE Transactions on Ultrasonics, Ferroelectrics, and Frequency Control, vol. 56, no. 4, pp. 779-787, April 2009, doi: 10.1109/TUFFC.2009.1100.

[4] R. T. Smith, F. S. Welsh; Temperature Dependence of the Elastic, Piezoelectric, and Dielectric Constants of Lithium Tantalate and Lithium Niobate. *J. Appl. Phys.* 1 May 1971; 42 (6): 2219–2230. https://doi.org/10.1063/1.1660528

[5] Trusty, Yuri & Khmeleva, Ekaterina & McGann, Jason & Hartz, Jequil & Emanetoglu, Nuri & Vetelino, John. (2023). A Room Temperature Compensated Lateral Field Excited Lithium Tantalate Sensor Platform. 1-4. 10.1109/IUS51837.2023.10307345.

[6] B. A. Auld, Acoustic Fields and Waves in Solids (John Wiley & Sons, Inc., Toronto, 1973), Vol. I.

[7] Jequil S. R. Hartz, Nuri W. Emanetoglu, Caitlin Howell, John F. Vetelino; Lateral field excited quartz crystal microbalances for biosensing applications. *Biointerphases* 1 May 2020; 15 (3): 030801. https://doi.org/10.1116/6.0000144

[8] J. Vetelino and A. Reghu, ”Introduction to Sensors” (CRC, Boca Raton, FL, 2011).

[9] F. Josse, “Acoustic wave liquid-phase-based microsensors,” Sens. Actuators A, vol. 44, no. 2, pp. 199–208, 1994.

[10] M. Rodahl, F. Hook, and B. Kasemo, “QCM operation in liquids: an explanation of the measured variations in frequency and Q factor with liquid conductivity,” Anal. Chem., vol. 68, no. 13, pp. 2219–2227, 1996.

[11] D. F. McCann, J. M. Parks, J. M. McGann, M. Pereira da Cunha and J. F. Vetelino, ”4D-5 Lateral Field Excited High Frequency Bulk Acoustic Wave Sensors,” 2007 IEEE Ultrasonics Symposium Proceedings, 2007, pp. 264-267, doi: 10.1109/ULT-SYM.2007.77.

[12] R. Bechmann, A.D. Ballato, T.J. Lukaszek, "Frequency-Temperature Behavior of Thickness Modes of Double-Rotated Quartz Plates," 15th Annual Symposium on Frequency Control. 1961, 1961, pp. 22-48. Available from: https://doi.org/10.1109/FREQ.1961.199468

[13] J. F. Rosenbaum, Bulk Acoustic Wave Theory and Devices (Artech House, Inc., Norwood, MA, 1988).

[14] T. Yamada, N. Niizeki, "Formulation of Admittance for Parallel Field Excitation of Piezoelectric Plates" in Journal of Applied Physics, vol. 41, no. 9, Aug.1970, pp. 3604-3609 Available from: http://doi.org/10.1063/1.1659478

[15] T. Yamada, N. Niizeki, "Admittance of piezoelectric plates vibrating under the perpendicular field excitation" in Proceedings of the IEEE, vol. 58, no. 6, June.1970, pp. 941-942 Available from: http://doi.org/10.1109/PROC.1970.7820

[16] A. Ballato, E.R. Hatch, M. Mizan, T.J. Lukaszek, “Lateral Field Equivalent Networks and Piezocoupling Factors of Quartz Plates Driven in Simple Thickness Modes,”in IEEE Transactions on Ultrasonics, Ferroelectrics, and Frequency Control, vol. 33, no. 4, July 1986, pp. 385-393. Available from: https://doi.org/10.1109/T-UFFC.1986.26846

[17] "IEEE Standard on Piezoelectricity," in ANSI/IEEE Std 176-1978 , vol., no., pp.1-58, 29 Sept. 1978, doi: 10.1109/IEEESTD.1978.8941331. keywords: {IEEE Standards;Piezoelectricity},

[18] Marion, J.B.: “Classical dynamics of particles and systems”, *Sec. Ed.*, Academic Press, 1970, pp 384-386

[19] Vasimalla, Yesudasu & Pradhan, Himansu & Pandya, Rahul. (2021). Recent progress in surface plasmon resonance based sensors: A comprehensive review. Heliyon. 7. e06321. 10.1016/j.heliyon.2021.e06321.

[20] Y. Hu, L. A. French, K. Radecsky, M. P. Dacunha, P. Millard, and J. F. Vetelino, in Proceedings of the IEEE International Ultrasonics Symposium, Honolulu, HI, 5–8 October 2003 (IEEE, Piscataway, NJ, 2003), pp. 46–51.

[21] M. Meissner, L. A. French, W. Pinkham, C. York, G. Bernhardt, M. Pereira Da Cunha, and J. F. Vetelino, in Proceedings of the IEEE International Ultrasonics Symposium, Montreal, QC, 23–27 August 2004 (IEEE, Piscataway, NJ, 2004), pp. 314–318.

[22] J. M. McGann, D. F. McCann and J. F. Vetelino, ”Lateral field excited LiTaO3 acoustic wave sensing platform,” 2010 IEEE International Ultrasonics Symposium, 2010, pp. 938-941, doi: 10.1109/ULTSYM.2010.5935758.

[23] C. York, L. A. French, P. Millard and J. F. Vetelino, ”A lateral field excited acoustic wave biosensor,” IEEE Ultrasonics Symposium, 2005., 2005, pp. 44-49, doi: 10.1109/ULTSYM.2005.1602792.

[24] W. Pinkham, M. Wark, S. Winters, L. French, D. J. Frankel and J. F. Vetelino, ”A lateral field excited acoustic wave pesticide sensor,” IEEE Ultrasonics Symposium, 2005., 2005, pp. 2279 2283, doi: 10.1109/ULTSYM.2005.1603339.

[25] L. A. French, D. F. McCann, M. Wark, S. Winters and J. F. Vetelino, "A Lateral Field Excited Acoustic Wave Sensor," TRANSDUCERS 2007 - 2007 International Solid-State Sensors, Actuators and Microsystems Conference, Lyon, France, 2007, pp. 1287-1290, doi: 10.1109/SENSOR.2007.4300373.

[26] Jiapu Li, Yuqing Ma, Tao Zhang, K. Kirk Shung, Benpeng Zhu. Recent Advancements in Ultrasound Transducer: From Material Strategies to Biomedical Applications. *BME Front.* 2022;2022:9764501.DOI:10.34133/2022/9764501

APPENDIX A: MATLAB SCRIPTS

$LiTaO_3$ Simulation Script

Main Program

"lithium_tantalate_simulation.m"

```
clear all;

syms vsqrd;                                 % Symbolic variable for
                                            % (phase velocity)^2
T0 = 25;                                    % Room temp
t0 = 0.0005;                                % Xstal thickness (room temp)
p0 = 7.454;                                 % Xstal density (room temp)
cap = 1e-9;                                 % Xstal capacitance
freq = 3000000:100:4000000;                 % Frequency vector
temp = -5:.1:55;                            % Temperature vector
theta = [-90:1:-85 -84.2 -84:1:90];         % Theta vector

% Elastic constants (unrotated, room temp)
c11_0 = 229.8;
c12_0 = 44;
c13_0 = 81.2;
c14_0 = -10.4;
c33_0 = 279.8;
c44_0 = 96.8;
c66_0 = 92.9;

% Piezoelectric constants (unrotated, room temp)
e15_0 = 2.72;
e22_0 = 1.67;
e31_0 = -0.38;
e33_0 = 1.09;

% Dielectric constants (unrotated, room temp)
E11_0 = 0.377;
E33_0 = 0.379;

% Elastic constant matrix (unrotated, room temp)
C0 = [c11_0  c12_0 c13_0  c14_0   0     0;
        c12_0  c11_0 c13_0 -c14_0   0     0;
        c13_0  c13_0 c33_0    0     0     0;
        c14_0 -c14_0   0    c44_0   0     0;
          0      0     0      0   c44_0 c14_0;
          0      0     0      0   c14_0 c66_0];
% Piezoelectric constant matrix (unrotated, room temp)
```

```
E0 = [   0      0      0     0    e15_0 -e22_0;
        -e22_0  e22_0    0   e15_0    0      0;
         e31_0  e31_0  e33_0   0      0      0];

% Dielectric constant matrix (unrotated, room temp)
Ep0 = [E11_0   0     0;
          0   E11_0   0;
          0     0   E33_0];
% Temperature coefficients of elastic constants
T1c11 = -1.03e-4;
T1c12 = -3.41e-4;
T1c13 = -0.50e-4;
T1c14 = 6.67e-4;
T1c33 = -0.96e-4;
T1c44 = -0.43e-4;
T1c66 = -0.47e-4;
T2c11 = 0.77e-7;
T2c12 = -1.18e-7;
T2c13 = 6.00e-7;
T2c14 = 16.7e-7;
T2c33 = -3.21e-7;
T2c44 = 1.67e-7;
T2c66 = 1.24e-7;
T3c11 = 0;
T3c12 = 0;
T3c13 = 0;
T3c14 = 0;
T3c33 = 0;
T3c44 = 0;
T3c66 = 0;

% Temperature coefficients of piezoelectric constants
T1e15 = -1.32e-4;
T1e22 = -0.6e-4;
T1e31 = 0.87e-4;
T1e33 = 1.54e-4;
T2e15 = -7.17e-7;
T2e22 = -6.28e-7;
T2e31 = 51.8e-7;
T2e33 = 1.41e-7;
T3e15 = 0;
T3e22 = 0;
T3e31 = 0;
T3e33 = 0;




% Temperature coefficients of dielectric constants
```

```
T1E11 = 3.29e-4;
T1E33 = 11.6e-4;
T2E11 = 4.28e-7;
T2E33 = 78e-7;
T3E11 = 0;
T3E33 = 0;

% Temperature coefficients of thermal expansion
T1a11 = 0.161e-4;
T1a33 = 0.041e-4;
T2a11 = 0.070e-7;
T2a33 = -0.100e-7;
T3a11 =0;
T3a33 =0;

%%

% Calculate material constants at each temperature
for j = 1:numel(temp)

      % Elastic constants at given temperature
      c11 = c11_0*(1 + T1c11*(temp(j)-T0) + T2c11*(temp(j)-T0)^2);
      c12 = c12_0*(1 + T1c12*(temp(j)-T0) + T2c12*(temp(j)-T0)^2);
      c13 = c13_0*(1 + T1c13*(temp(j)-T0) + T2c13*(temp(j)-T0)^2);
      c14 = c14_0*(1 + T1c14*(temp(j)-T0) + T2c14*(temp(j)-T0)^2);
      c33 = c33_0*(1 + T1c33*(temp(j)-T0) + T2c33*(temp(j)-T0)^2);
      c44 = c44_0*(1 + T1c44*(temp(j)-T0) + T2c44*(temp(j)-T0)^2);
      c66 = c66_0*(1 + T1c66*(temp(j)-T0) + T2c66*(temp(j)-T0)^2);

      C0 = [c11  c12 c13  c14  0   0;
              c12  c11 c13 -c14  0   0;
              c13  c13 c33   0   0   0;
              c14 -c14  0   c44  0   0;
               0    0   0    0  c44 c14;
               0    0   0    0  c14 c66];

      % Piezoelectric constants at given temperature
      e15 = e15_0*(1 + T1e15*(temp(j)-T0) + T2e15*(temp(j)-T0)^2);
      e22 = e22_0*(1 + T1e22*(temp(j)-T0) + T2e22*(temp(j)-T0)^2);
      e31 = e31_0*(1 + T1e31*(temp(j)-T0) + T2e31*(temp(j)-T0)^2);
      e33 = e33_0*(1 + T1e33*(temp(j)-T0) + T2e33*(temp(j)-T0)^2);

      E0 = [  0   0   0   0  e15 -e22;
              -e22 e22  0  e15  0    0;
               e31 e31 e33  0   0    0 ];



      % Dielectric constants at given temperature
```

```
E11 = E11_0*(1 + T1E11*(temp(j)-T0) + T2E11*(temp(j)-T0)^2);
E33 = E33_0*(1 + T1E33*(temp(j)-T0) + T2E33*(temp(j)-T0)^2);

Ep0 = [E11  0   0;
       0  E11  0;
       0   0  E33];

% Apply temperature coefficients to xstal thickness and density
t(j) = t0*(1 + T1a33*(temp(j)-T0) + T2a33*(temp(j)-T0)^2);
p(j) = p0*(1 - (T1a11 + T1a11 + T1a33)*(temp(j)-T0) - (T2a11 + T2a11
          + T2a33)*(temp(j)-T0)^2);



% Rotate xstal material constants and calculate phase velocities,
% coupling, and frequency response at each orientation
for k = 1:numel(theta)

      [C, E, Ep] = rotate_crystal(C0, E0, Ep0, 0, theta(k), 0);

      % Phase velocities
      % Build 'A' matrix
      a = C(6,6) + E(2,6)*E(2,6)/Ep(2,2) - p(j)*vsqrd;
      b = C(6,2) + E(2,6)*E(2,2)/Ep(2,2);
      c = C(6,4) + E(2,6)*E(2,4)/Ep(2,2);
      d = C(2,6) + E(2,2)*E(2,6)/Ep(2,2);
      e = C(2,2) + E(2,2)*E(2,2)/Ep(2,2) - p(j)*vsqrd;
      f = C(2,4) + E(2,2)*E(2,4)/Ep(2,2);
      g = C(4,6) + E(2,4)*E(2,6)/Ep(2,2);
      h = C(4,2) + E(2,4)*E(2,2)/Ep(2,2);
      i = C(4,4) + E(2,4)*E(2,4)/Ep(2,2) - p(j)*vsqrd;

      A = [a b c; d e f; g h i];

      % Take determinant, find roots
      determ = det(A);
      D = sym2poly(determ);
      R = roots(D);

      % Calculate phase velocities
      V{j}(1,k) = sqrt(R(1));
      V{j}(2,k) = sqrt(R(2));
      V{j}(3,k) = sqrt(R(3));




      % Electromechanical coupling
```

```
% Remove velocity terms from 'A' matrix
a = C(6,6) + E(2,6)*E(2,6)/Ep(2,2);
b = C(6,2) + E(2,6)*E(2,2)/Ep(2,2);
c = C(6,4) + E(2,6)*E(2,4)/Ep(2,2);
d = C(2,6) + E(2,2)*E(2,6)/Ep(2,2);
e = C(2,2) + E(2,2)*E(2,2)/Ep(2,2);
f = C(2,4) + E(2,2)*E(2,4)/Ep(2,2);
g = C(4,6) + E(2,4)*E(2,6)/Ep(2,2);
h = C(4,2) + E(2,4)*E(2,2)/Ep(2,2);
i = C(4,4) + E(2,4)*E(2,4)/Ep(2,2);

A = [a b c; d e f; g h i];

% Find eigenvectors and eigenvalues
[beta,cm] = eig(A);

[cm1,ind] = sort(diag(cm));

beta = beta(:,ind);

% Calculate TFE coupling
kte2{j}(1,k) = ((E(2,6)*beta(1,3) + E(2,2)*beta(2,3)
                 + E(2,4)*beta(3,3))^2) / (Ep(2,2)*cm1(3));
kte2{j}(2,k) = ((E(2,6)*beta(1,2) + E(2,2)*beta(2,2)
                 + E(2,4)*beta(3,2))^2) / (Ep(2,2)*cm1(2));
kte2{j}(3,k) = ((E(2,6)*beta(1,1) + E(2,2)*beta(2,1)
                 + E(2,4)*beta(3,1))^2) / (Ep(2,2)*cm1(1));

kte{j}(1,k) = sqrt(kte2{j}(1,k));
kte{j}(2,k) = sqrt(kte2{j}(2,k));
kte{j}(3,k) = sqrt(kte2{j}(3,k));

% Calculate LFE coupling
numer(1) = (((E(1,6) - E(2,6)*(Ep(1,2)/Ep(2,2)))*beta(1,3))
             + ((E(1,2) - E(2,2)*(Ep(1,2)/Ep(2,2)))*beta(2,3))
             + ((E(1,4)
             - E(2,4)*(Ep(1,2)/Ep(2,2)))*beta(3,3)))^2;

denom(1) = (Ep(1,1) - ((Ep(1,2)^2)/Ep(2,2)))*cm1(3);

numer(2) = (((E(1,6) - E(2,6)*(Ep(1,2)/Ep(2,2)))*beta(1,2))
             + ((E(1,2) - E(2,2)*(Ep(1,2)/Ep(2,2)))*beta(2,2))
             + ((E(1,4)
             - E(2,4)*(Ep(1,2)/Ep(2,2)))*beta(3,2)))^2;

denom(2) = (Ep(1,1) - ((Ep(1,2)^2)/Ep(2,2)))*cm1(2);



numer(3) = (((E(1,6) - E(2,6)*(Ep(1,2)/Ep(2,2)))*beta(1,1))
```

```
              + ((E(1,2) - E(2,2)*(Ep(1,2)/Ep(2,2)))*beta(2,1))
              + ((E(1,4)
              - E(2,4)*(Ep(1,2)/Ep(2,2)))*beta(3,1)))^2;

denom(3) = (Ep(1,1) - ((Ep(1,2)^2)/Ep(2,2)))*cm1(1);

kle2{j}(1,k) = numer(1)/denom(1);
kle2{j}(2,k) = numer(2)/denom(2);
kle2{j}(3,k) = numer(3)/denom(3);
kle{j}(1,k) = sqrt(kle2{j}(1,k));
kle{j}(2,k) = sqrt(kle2{j}(2,k));
kle{j}(3,k) = sqrt(kle2{j}(3,k));


% Calculate TFE (impedance) and LFE (admittance) frequency
% response
for n = 1:numel(freq)

      w = freq(n)*2*pi;       % Angular frequency
      w = w/2;                % Largest allowed wavelength is
                              % 2*crystal thickness

      Za{j}(k,n) =
                  (kte2{j}(1,k)*tan(w*t(j)/(V{j}(1,k)*1000))/(w*t
                  (j)/(V{j}(1,k)*1000)));
      Zb{j}(k,n) =
                  (kte2{j}(2,k)*tan(w*t(j)/(V{j}(2,k)*1000))/(w*t
                  (j)/(V{j}(2,k)*1000)));
      Zc{j}(k,n) =
                  (kte2{j}(3,k)*tan(w*t(j)/(V{j}(3,k)*1000))/(w*t
                  (j)/(V{j}(3,k)*1000)));

      Zsum{j}(k,n) = Za{j}(k,n) + Zb{j}(k,n) + Zc{j}(k,n);
      Zte{j}(k,n) = (1/(1i*w*cap))*(1 - Zsum{j}(k,n));

      Ya{j}(k,n) =
                  (kle2{j}(1,k)*tan(w*t(j)/(V{j}(1,k)*1000))/(w*t
                  (j)/(V{j}(1,k)*1000)));
      Yb{j}(k,n) =
                  (kle2{j}(2,k)*tan(w*t(j)/(V{j}(2,k)*1000))/(w*t
                  (j)/(V{j}(2,k)*1000)));
      Yc{j}(k,n) =
                  (kle2{j}(3,k)*tan(w*t(j)/(V{j}(3,k)*1000))/(w*t
                  (j)/(V{j}(3,k)*1000)));

      Ysum{j}(k,n) = Ya{j}(k,n) + Yb{j}(k,n) + Yc{j}(k,n);
      Yle{j}(k,n) = 1i*w*cap*(1 + Ysum{j}(k,n));
end

% Identify resonant frequency
```

```
            [M,ind] = max(mag2db(abs(Yle{j}(k,:))));
            Yres(j,k) = freq(ind);
      end
end

% Calculate resonant frequency shifts (PPM) from resonance at room temp
for j = 1:numel(temp)
      for k = 1:numel(theta)
            Yshift(j,k) = ((Yres(j,k)-
Yres(find(temp==25),k))./Yres(find(temp==25),k)).*1e6;
      end
end

%%

% Plot phase velocities, TFE coupling, and LFE coupling for each acoustic
% mode at each crystal orientation
figure;
plot(theta, V{find(temp==25)}(1,:));
hold on;
plot(theta, V{find(temp==25)}(2,:));
plot(theta, V{find(temp==25)}(3,:));
legend("a (longitudinal) mode", "b (fast shear) mode", "c (slow shear)
mode");
xlabel("\theta [°]");
ylabel("Velocity [km/s]");
title("Acoustic Mode Velocities with Respect to \theta");
grid on;

figure;
plot(theta, kte{find(temp==25)}(1,:));
hold on;
plot(theta, kte{find(temp==25)}(2,:));
plot(theta, kte{find(temp==25)}(3,:));
legend("a (longitudinal) mode", "b (fast shear) mode", "c (slow shear)
mode");
xlabel("\theta [°]");
ylabel("TFE Coupling");
title("TFE Electromechanical Coupling with Respect to \theta");
grid on;

figure;
plot(theta, kle{find(temp==25)}(1,:));
hold on;
plot(theta, kle{find(temp==25)}(2,:));
plot(theta, kle{find(temp==25)}(3,:));
legend("a (longitudinal) mode", "b (fast shear) mode", "c (slow shear)
mode");
xlabel("\theta [°]");
ylabel("LFE Coupling");
```

```
title("LFE Electromechanical Coupling With Respect to \theta");
grid on;

% Plot TFE and LFE frequency responses
figure;
plot(freq,mag2db(abs(Zte{find(temp==25)}(find(theta==-84.2),:))));
xlabel("Frequency [Hz]");
ylabel("|Impedance| [dB]");
title("(YXwl) 0°/-84.2° TFE Impedance Response");
grid on;

figure;
plot(freq,mag2db(abs(Yle{find(temp==25)}(find(theta==-84.2),:))));
xlabel("Frequency [Hz]");
ylabel("|Admittance| [dB]");
title("(YXwl) 0°/-84.2° LFE Admittance Response");
grid on;

figure
plot(temp,Yshift(:,find(theta==-84.2)));
xlabel("Temperature [°C]");
ylabel("Resonant Frequency Shift [PPM]");
title("(YXwl) 0°/-84.2° LFE Resonant Frequency Shift vs. Temperature");
grid on;
```

Crystal Rotation Function

“rotate_crystal.m”

```
function [c,e,epsilon] =
rotate_crystal(c_orig,e_orig,epsilon_orig,phi_deg,theta_deg,psi_deg)

phi=phi_deg*pi/180.0;
theta=theta_deg*pi/180.0;
psi=psi_deg*pi/180.0;

c=zeros(size(c_orig));
e=zeros(size(e_orig));
epsilon=zeros(size(epsilon_orig));

% Necessary Euler transformations
V=[1,0,0;0,1,0;0,0,1];
V(1,1)=cos(phi)*cos(psi)-sin(phi)*cos(theta)*sin(psi);
V(1,2)=sin(phi)*cos(psi)+cos(phi)*cos(theta)*sin(psi);
V(1,3)=sin(theta)*sin(psi);
V(2,1)=-cos(phi)*sin(psi)-sin(phi)*cos(theta)*cos(psi);
V(2,2)=-sin(phi)*sin(psi)+cos(phi)*cos(theta)*cos(psi);
V(2,3)=sin(theta)*cos(psi);
V(3,1)=sin(phi)*sin(theta);
V(3,2)=-cos(phi)*sin(theta);
V(3,3)=cos(theta);

% Epsilon transformation
for m_prime=1:1:3
      for n_prime=1:1:3
            val=0.0;
            for m=1:1:3
                  for n=1:1:3
                        val=val+V(m_prime,m)*V(n_prime,n)*epsilon_orig(m,n);
                  end
            end
            epsilon(m_prime,n_prime)=val;
      end
end



% Piezoelectric transformation
for m_prime=1:1:3
      for k_prime=1:1:3
            for l_prime=1:1:3
                  val=0.0;
                  for m=1:1:3
                        for k=1:1:3
```

```
                              for l=1:1:3
                                    val=val+V(m_prime,m)
                                        *V(k_prime,k)*V(l_prime,l)
                                        *e_orig(m,tensor2matind(k,l));
                              end
                        end
                  end
                  e(m_prime,tensor2matind(k_prime,l_prime))=val;
            end
      end
end

% Stiffness transformation
for i_prime=1:1:3
      for j_prime=1:1:3
            for k_prime=1:1:3
                  for l_prime=1:1:3
                        val=0.0;
                        for i=1:1:3
                              for j=1:1:3
                                    for k=1:1:3
                                          for l=1:1:3
                                                val=val+V(i_prime,i)
                                                  *V(j_prime,j)*V(k_prime,k)
                                                  *V(l_prime,l)
                                                  *c_orig(tensor2matind(i,j),
                                                   tensor2matind(k,l));
                                          end
                                    end
                              end
                        end

      c(tensor2matind(i_prime,j_prime),tensor2matind(k_prime,l_prime))=val;
                  end
            end
      end
end
return
```

Voight Indices Conversion Function

“tensor2matind.m”

```
function I  = tensor2matind(i,j)

if (i==1 & j==1)
      I=1;
elseif(i==2 & j==2)
      I=2;
elseif(i==3 & j==3)
      I=3;
elseif((i==2 & j==3) | (i==3 & j==2))
      I=4;
elseif((i==1 & j==3) | (i==3 & j==1))
      I=5;
elseif((i==1 & j==2) | (i==2 & j==1))
      I=6;
end
```

Temperature Response Measurement Automation Script

```
%% VNA setup: pre-calibration.
%  Initial configuration of VNA and measurement channels.
%

instrreset;             % Remove all interfaces to instruments.
oldobjs = instrfind;    % Find all previously created objects.

if (~isempty(oldobjs))  % If any existing objects,
fclose(oldobjs);        % close connection to instrument,
delete(oldobjs);        % free up object resources.
end

clear oldobjs;          % Remove object list from workspace.

% Define VNA interface.
% 'vendor' and 'VISA_resource_name' are device-specific.
VNA = visa('agilent', 'USB0::0x0957::0x0D09::MY46102374::0::INSTR');

set(VNA,'InputBufferSize', 640e3);        % Set buffer sizes.
set(VNA,'OutputBufferSize', 640e3);       % Must precede open command.

fopen(VNA);                   % Connect to instrument. Open session.
fprintf(VNA, '*CLS');         % Clear error queue, event status registers.
fprintf(VNA, 'SYST:ERR?');    % Check error queue is clear.
err = fscanf(VNA, '%c');      % Should be '+0, "No Error"'.
fprintf(strcat('\nInitial error:',err,'\n'));

fprintf(VNA, '*IDN?');                    % Query instrument ID string.
idn = fscanf(VNA, '%c');
fprintf(strcat('ID:\t',idn,'\n'));

% set(VNA, 'Timeout', 15);    % 15 second timeout for longer sweep times.
set(VNA, 'Timeout', 360);     % 360 second timeout for longer sweep times.
% fprintf(VNA, 'DISP:SPL D123456'); % Create 4 channels, 1 for each harmonic.

%%%%%%%%% THE FOLLOWING CHANGE FREQUENTLY. ADJUSTING MANUALLY FOR NOW.
% r = 3.54e6;                                   % LTO fundamental resonance.
% h = [5,7,9,11];                               % LTO harmonics.
%
% for i = 1:4
%     fprintf(VNA, "DISP:WIND"+i+":ACT");       % Select channel.
%     fprintf(VNA, "CALC"+i+":PAR:DEF S22");    % Configure S-parameters.
%     fprintf(VNA, "SENS"+i+":SWE:POIN 1601");        % Set sweep points.
%     fprintf(VNA, "SENS"+i+":FREQ:CENT "+r*h(i));    % Center on resonance.
%     fprintf(VNA, "SENS"+i+":FREQ:SPAN 3200000");    % Set span for
                                                      % calibration.
%     fprintf(VNA, "SENS"+i+":BAND 100");       % Set IFBW for calibration.
%     fprintf(VNA, "DISP:WIND"+i+":TRAC:Y:AUTO");     % Autoscale.
```

```
% end

%% Calibrate VNA.

%% VNA setup: post-calibration.
%  Finish configuration of measurement channels.
%

% THE FOLLOWING CHANGE FREQUENTLY. ADJUSTING MANUALLY FOR NOW.
% for i = 1:4
%     fprintf(VNA, "CALC"+i+":SEL:CONV:STAT ON");     % Conversion on.
%     fprintf(VNA, "CALC"+i+":SEL:CONV:FUNC YREF");   % Y:Reflection on.
%     fprintf(VNA, "SENS"+i+":FREQ:SPAN 1600000");    % Set span for
                                                      % measurement.
%     fprintf(VNA, "SENS"+i+":BAND 1000");      % Set IFBW for measurement.
%     fprintf(VNA, "CALC"+i+":MARK1:ACT");      % Set marker.
%     fprintf(VNA, "INIT"+i+":CONT ON");        % Continuous on.
% end

fprintf(VNA, 'TRIG:SOUR BUS');      % Trigger mode set to initiate
                                    % continuous on and trigger source as
                                    % bus.

%% RTD setup.
%  Configure serial communication to read measurements from resistance
%  temperature detector (RTD), transmitted by Omega CNi32 controller via
%  RS-232C.
%

% Find a serial port object.
RTD = instrfind('Type', 'serial', 'Port', 'COM5', 'Tag', '');

if isempty(RTD)                             % If it does not exist,
    RTD = serial('COM5');                   % create serial port object.
else
    fclose(RTD);                            % Otherwise,
    RTD = RTD(1);                           % use object that was found.
end

set(RTD, 'DataBits', 7);            % Configure number of data bits.
set(RTD, 'Terminator', {'CR','CR'});% Read, write terminator characters.

fopen(RTD);                         % Connect to serial port object.

%% PID setup.
%  Configure serial communication to transmit commands to Omega CNi-16 PID
%  controller via RS-232C to adjust temperature setpoint values.
%

% Find a serial port object.
```

```
PID = instrfind('Type', 'serial', 'Port', 'COM4', 'Tag', '');

if isempty(PID)                                 % If it does not exist,
    PID = serial('COM4');                       % create serial port object.
else
    fclose(PID);                                % Otherwise,
    PID = PID(1);                               % use object that was found.
end

set(PID, 'DataBits', 7);                        % Configure number of data
bits.
set(PID, 'Parity', 'odd');          % Configure parity.
set(PID, 'Terminator', {'CR','CR'});% Read, write terminator characters.

fopen(PID);                         % Connect to serial port object.

%% Measurement.

flushinput(RTD);                    % Clear old temperature data from buffer.
pause(1);
% tempread = fscanf(RTD);           % Get current (room) temperature.
% tempread = str2double(tempread);  % Convert from ASCII to double.
% tempread = floor(tempread);       % Round down to nearest integer.
%
% rmtemp = tempread;          % Actual temp varies. May either set to real
%                             % current temp (tempread) or manually
%                             % set (25, 26, etc).
% rmtemp = 26;

rmtemp = 25;
% start_temp = 25;
start_temp = 40;

dectemp = [1:rmtemp (rmtemp+1):95];       % Decimal temp vector.
hextemp = dec2hex(dectemp*100, 4);        % Hexadecimal temp vector.

setpoint = strcat('*W0230',hextemp);      % Temp setpoint commands.
reset = '*Z02';                           % Reset command.

tempset = start_temp;                     % Initial setpoint.
% tempinc = 30-rmtemp;                    % Initial temp ramping increment.
tempinc = 2;
soak = 360;                               % Soak time (minutes).
% soak = 12;

% Set initial setpoint, begin ramp.
% pause(60*60);
fprintf(PID, setpoint(tempset,:));
pause(1);
fprintf(PID, reset);
```

```
pause(1);
timestrtrmp = clock;    % Save ramp start time in case needed.

while (1)

      % Read current temperature.
      pause(1);
      flushinput(RTD);
      pause(1);
      time = clock;
      tempread = fscanf(RTD);
      tempread = str2double(tempread);

      % Condition for beginning of soak. Uncomment one. Change if desired.
      % Begin soak when temp 5% below setpoint.
      % if ((tempset*0.95) <= tempread)
      % Begin soak when temp 0.5 degree below setpoint.
    if (tempset == 1)
        if ((tempset+0.5) >= tempread)

            % First half of soak ("presoak") spent only tracking time
            % and temp.
            presoak{1,1} = time;
            presoak{1,2} = tempread;
            count = 2;
            strt = tic;
            stop = toc(strt);
            while (stop < soak*60/6)
                pause(59);
                flushinput(RTD);
                pause(1);
                presoak{count,1} = clock;
                tempread = fscanf(RTD);
                presoak{count,2} = str2double(tempread);
                count = count+1;
                stop = toc(strt);
            end


            save("PRESOAK_LTO_BLK_CN_90_2C_360MIN_UP_"+dectemp(tempset)+".mat
            ",'presoak');

            % Second part of soak spent tracking time, temp, sample response.
            count = 1;
            strt = tic;
            stop = toc(strt);
            while (stop < ((soak*(5/6))*60))
            % pause(1);
                flushinput(RTD);
                data{1,1} = clock;
```

```
tempread = fscanf(RTD);
data{1,2} = str2double(tempread);
data{1,15} = err;                       % Keep track of error
                                        % codes.

fprintf(VNA, 'TRIG:SING;*OPC?');        % Trigger sweep, wait
                                        % for completion
opComplete = fscanf(VNA, '%s');         % via *OPC? (operation
                                        % complete) query.
pause(2);
fprintf(VNA,'FORM:BORD SWAP');  % Swap byte order on data
                                % query return.
pause(1);
fprintf(VNA, 'FORM:DATA REAL'); % Set Trace Data read
                                % return format as bin
                                % block real 64-bit values.

j = 2;
for i = 1:6         % Get data from each channel/harmonic.

  pause(2);
  fprintf(VNA, "CALC"+i+":PAR:SEL");% Select trace to read.
  pause(1);

  % MAGNITUDE.
  fprintf(VNA, "CALC"+i+":DATA:FDATA?");    % Query magnitude
  mag = binblockread(VNA, 'float64'); % data as bin
                                      % block real 64-
                                      % bit values.
  fscanf(VNA, '%c');      % Remove hanging linefeed
                          % left from binblockread().

  % FREQUENCY.
  fprintf(VNA, "SENS"+i+":FREQ:DATA?");     % Query frequency
  freq = binblockread(VNA, 'float64');      % data as bin
                                            % block real 64-
                                            % bit vals
  fscanf(VNA, '%c');      % Remove hanging linefeed
                          % left from binblockread

  % PHASE
  pause(1);
  fprintf(VNA, "CALC"+i+":SEL:FORM PHAS");  % Format channels
                                            % to read phase.
  pause(1);
  fprintf(VNA, "CALC"+i+":DATA:FDATA?");    % Query magnitude
  phase = binblockread(VNA, 'float64');     % data as bin
                                            % block real 64-
                                            % bit values.
  fscanf(VNA, '%c');      % Remove hanging linefeed
```

```
                                        % left from binblockread().

                pause(1);
                fprintf(VNA, "CALC"+i+":SEL:FORM MLOG");  % Format channels
                                                          % for magnitude.
                pause(1);


                fprintf(VNA, 'SYST:ERR?');    % Check for errors.
                err = fscanf(VNA, '%c');

                % Save data.
                data{1,i+j} = freq;
                data{1,i+j+1} = mag(1:2:end);
                data{1,i+j+2} = phase(1:2:end);
                data{i,15} = err;

                j = j+1;
            end

            save("LTO_BLK_CN_90_2C_360MIN_UP_"+dectemp(tempset)+"_"+count+".m
            at",'data');

            count = count+1;
            stop = toc(strt);
        end

            tempset = tempset+tempinc;    % Increment setpoint.

            % If increment is 0, final (31C) soak, and entire ramp, is
completed.
            if (tempinc == 0)
                break;

            % If increment is not 0 and not 2, first soak has
            % finished. Switch to consistent 2 degree increments.
            elseif (tempinc ~= 2)
                tempinc = 2;
            end

            % If final (70C) setpoint about to begin, set increment to 0 to
            % pass condition above.
            if (tempset == 70)
                tempinc = 0;
            end

            % Set next setpoint.
            fprintf(PID, setpoint(tempset,:));
            pause(1);
            fprintf(PID, reset);
```

```
            pause(1);
        end

    elseif ((tempset-0.5) <= tempread)

            % First part of soak ("presoak") spent only tracking time and
temp.
            presoak{1,1} = time;
            presoak{1,2} = tempread;
            count = 2;
            strt = tic;
            stop = toc(strt);
            while (stop < soak*60/6)
                  pause(59);
                  flushinput(RTD);
                  pause(1);
                  presoak{count,1} = clock;
                  tempread = fscanf(RTD);
                  presoak{count,2} = str2double(tempread);
                  count = count+1;
                  stop = toc(strt);
            end


      save("PRESOAK_LTO_BLK_CN_90_2C_360MIN_UP_"+dectemp(tempset)+".mat",'pre
soak');

            % Second half of soak spent tracking time, temp, sample response.
            count = 1;
            strt = tic;
            stop = toc(strt);
            while (stop < ((soak*(5/6))*60))
%                 pause(1);
                  flushinput(RTD);
%                 pause(1);
                  data{1,1} = clock;
                  tempread = fscanf(RTD);
                  data{1,2} = str2double(tempread);
                  data{1,15} = err;                   % Keep track of error
codes.

                  fprintf(VNA, 'TRIG:SING;*OPC?');    % Trigger sweep, wait
for completion
                  opComplete = fscanf(VNA, '%s');     % via *OPC? (operation
complete) query.
                  pause(2);
                  fprintf(VNA,'FORM:BORD SWAP');      % Swap byte order on
data query return.
                  pause(1);
```

```
                  fprintf(VNA, 'FORM:DATA REAL');     % Set Trace Data read
or return format
                                                      % as bin block real 64-bit
values.

                  j = 2;
                  for i = 1:6       % Get data from each channel/harmonic.

                        pause(2);
                        fprintf(VNA, "CALC"+i+":PAR:SEL");        % Select
trace to read.
                        pause(1);

                        % MAGNITUDE.
                        fprintf(VNA, "CALC"+i+":DATA:FDATA?");    % Query
magnitude data as bin
                        mag = binblockread(VNA, 'float64');       % block
real 64-bit values.
                        fscanf(VNA, '%c');
      % Remove hanging linefeed

      % left from binblockread().
                        % FREQUENCY.
                        fprintf(VNA, "SENS"+i+":FREQ:DATA?");     % Query
frequency data as
                        freq = binblockread(VNA, 'float64');      % bin block
real 64-bit vals
                        fscanf(VNA, '%c');
      % Remove hanging linefeed

      % left from binblockread
                        % PHASE
%                       pause(1);
%                       fprintf(VNA, "CALC"+i+":SEL:FORM PHAS");% Format
channels to read phase.
%                       pause(1);
%                       fprintf(VNA, "CALC"+i+":DATA:FDATA?");    % Query
magnitude data as bin
%                       phase = binblockread(VNA, 'float64');     % block
real 64-bit values.
%                       fscanf(VNA, '%c');
      % Remove hanging linefeed
%
      % left from binblockread().
%
%                       pause(1);
%                       fprintf(VNA, "CALC"+i+":SEL:FORM MLOG");% Format
channels for magnitude.
%                       pause(1);
```

```
                        fprintf(VNA, 'SYST:ERR?');                          %
Check for errors.
                        err = fscanf(VNA, '%c');

                        % Save data.
                        data{1,i+j} = freq;
                        data{1,i+j+1} = mag(1:2:end);
%                       data{1,i+j+2} = phase(1:2:end);
                        data{i,15} = err;

%                       j = j+2;
                j = j+1;
                  end


      save("LTO_BLK_CN_90_2C_360MIN_UP_"+dectemp(tempset)+"_"+count+".mat",'d
ata');
                  count = count+1;
            stop = toc(strt);
            end

            tempset = tempset+tempinc;    % Increment setpoint.

            % If increment is 0, final (70C) soak, and entire ramp, is
completed.
            if (tempinc == 0)
                  break;

            % If increment is not 0 and not 2, first soak has
            % finished. Switch to consistent 2 degree increments.
            elseif (tempinc ~= 2)
                  tempinc = 2;
            end

            % If final (70C) setpoint about to begin, set increment to 0 to
            % pass condition above.
            if (tempset == 70)
                  tempinc = 0;
            end

            % Set next setpoint.
            fprintf(PID, setpoint(tempset,:));
            pause(1);
            fprintf(PID, reset);
            pause(1);
    end
end

% Upwards ramp completed. Set room temp setpoint, allow system to cool.
tempset = rmtemp;
```

```
fprintf(PID, setpoint(tempset,:));
pause(1);
fprintf(PID, reset);
pause(1);

%%%%%%%%%%%%%%%%%%%%%%%%%%%%%%%% CLEANUP
%%%%%%%%%%%%%%%%%%%%%%%%%%%%%%%%%%%%%%%%

% Return data transfer format back to ASCII string format.
fprintf(VNA, 'FORM:DATA ASCII');

% Return trigger source to internal and free running.
fprintf(VNA, 'TRIG:SOUR INT');

% Close ENA session connection
fclose(VNA);
delete(VNA);
clear VNA;

% Disconnect from PID controller instrument object.
fclose(PID);
delete(PID);
clear PID;

fclose(RTD);
delete(RTD);
clear RTD;
```

BIOGRAPHY OF THE AUTHOR

Yuri Trusty was born in Bangor, Maine on May 9, 1989. He graduated from Bangor High School in 2007. In 2022 he graduated from the University of Maine with dual bachelor's degrees in electrical and computer engineering. His thesis work as a University of Maine graduate student was presented and published in the 2023 IEEE International Ultrasonics Symposium. He is a member of Tau Beta Pi and Eta Kappa Nu engineering societies. He is currently employed by Diodes Incorporated as a thin films semiconductor process engineer. Yuri is a candidate for the Master of Science degree in Electrical Engineering from the University of Maine in August 2024.